EXPERIMENTAL DATA IN SUPPORT OF

A MAGNETIC-GUIDEWAY/GUIDED-PROJECTILE SYSTEM

CONCEPT FOR AEROBALLISTIC RANGES

VON KÁRMÁN GAS DYNAMICS FACILITY
ARNOLD ENGINEERING DEVELOPMENT CENTER
AIR FORCE SYSTEMS COMMAND
ARNOLD AIR FORCE STATION, TENNESSEE 37389

February 1977

Final Report for Period July 1973 — September 1976

Approved for public release; distribution unlimited.

Prepared for

DIRECTORATE OF TECHNOLOGY (DY)
ARNOLD ENGINEERING DEVELOPMENT CENTER
ARNOLD AIR FORCE STATION, TENNESSEE 37389

This report has been reviewed by the Information Office (OI) and is releasable to the National Technical Information Service (NTIS). At NTIS, it will be available to the general public, including foreign nations.

APPROVAL STATEMENT

This technical report has been reviewed and is approved for publication.

FOR THE COMMANDER

WILLIAM E. COLE
Captain, USAF
Requirements Planning Division
Directorate of Technology

ROBERT O. DIETZ
Director of Technology

REPORT DOCUMENTATION PAGE		READ INSTRUCTIONS BEFORE COMPLETING FORM
1 REPORT NUMBER AEDC-TR-76-148	2 GOVT ACCESSION NO.	3 RECIPIENT'S CATALOG NUMBER
4 TITLE (and Subtitle) EXPERIMENTAL DATA IN SUPPORT OF A MAGNETIC-GUIDEWAY/GUIDED-PROJECTILE SYSTEM CONCEPT FOR AEROBALLISTIC RANGES		5 TYPE OF REPORT & PERIOD COVERED Final Report – July 1973 September 1976
		6 PERFORMING ORG REPORT NUMBER
7 AUTHOR(s) G. D. Arney, Jr. and C. W. Pender, Jr. ARO, Inc.		8 CONTRACT OR GRANT NUMBER(s)
9 PERFORMING ORGANIZATION NAME AND ADDRESS Arnold Engineering Development Center (DY) Air Force Systems Command Arnold Air Force Station, Tennessee 37389		10 PROGRAM ELEMENT, PROJECT, TASK AREA & WORK UNIT NUMBERS Program Element 65807F
11 CONTROLLING OFFICE NAME AND ADDRESS Arnold Engineering Development Center (DYFS) Arnold Air Force Station Tennessee 37389		12 REPORT DATE February 1977
		13 NUMBER OF PAGES 72
14 MONITORING AGENCY NAME & ADDRESS(if different from Controlling Office)		15 SECURITY CLASS (of this report) UNCLASSIFIED
		15a DECLASSIFICATION DOWNGRADING SCHEDULE N/A

16 DISTRIBUTION STATEMENT (of this Report)

Approved for public release; distribution unlimited.

17 DISTRIBUTION STATEMENT (of the abstract entered in Block 20, if different from Report)

18 SUPPLEMENTARY NOTES

Available in DDC

19 KEY WORDS (Continue on reverse side if necessary and identify by block number)

guided projectile
magnetic projectile guidance
aeroballistics ranges

theory
force prediction
experimental

20 ABSTRACT (Continue on reverse side if necessary and identify by block number)
Two types of experiments have been conducted to determine adequacy of theory relative to a previously reported system concept for the incorporation of magnetic projectile guidance into aeroballistic ranges. The concept is based on motion-induced electrodynamic interactions between conductive material in the forebody of projectiles and a guideway of field source currents. By using a rotating machinery apparatus, one set of experiments was

DD FORM 1473 1 JAN 73   EDITION OF 1 NOV 65 IS OBSOLETE

20.   ABSTRACT (Continued)

conducted to simulate the interaction between a projectile fore-
body and the guideway currents to the extent that predicted
positional forces could be measured. These forces which are
intended to act toward the guideway axis as a function of lateral
forebody position were in agreement with theory. Through use of
a pendulum apparatus, another set of experiments was conducted to
simulate interactions to the extent that predicted damping forces
as needed for retardation of lateral forebody motion could be
measured. Again, the results were in agreement with theoretical
predictions.

AFSC
Arnold AFS Tenn

PREFACE

The research reported herein was conducted by the Arnold Engineering Development Center (AEDC), Air Force Systems Command (AFSC), under Program Element 65807F. The results presented were obtained by ARO, Inc., AEDC Division (a Sverdrup Corporation Company), operating contractor of AEDC, AFSC, Arnold Air Force Station, Tennessee. The work was done under ARO Project Numbers VF444-11GA, V31S-35A, V31S-04A, and V31S-A3A. The authors of this report were G. D. Arney, Jr., and C. W. Pender, Jr., ARO, Inc. The manuscript (ARO Control No. ARO-VKF-TR-76-111) was submitted for publication on September 29, 1976.

CONTENTS

ILLUSTRATIONS

APPENDIXES

1.0 INTRODUCTION

The results of two sets of experiments conducted in support of a magnetic-guideway/guided-projectile system concept for aeroballistic ranges are presented. A description and the theoretical aspects of the concept have previously been presented in Ref. 1. The intent of the experimental program has been to simulate the conditions under which the projectile is influenced by the guideway and to measure the simulated "guidance" forces for verification of theory.

In one set of experiments, the objective was to simulate the conditions under which the projectile experiences a positional force, i.e., that component of the guidance force that acts toward the guideway axis in an amount proportional to displacement therefrom. Such positional forces are generated electrodynamically by virtue of the projectile's rapid downrange velocity past positional elements of the guideway. Simulation of the necessary conditions has been accomplished to a reasonable degree by placing scaled-down positional guideway elements near the periphery of a large wheel and rotating the wheel at high speed. This effectively creates a traveling guideway with a stationary projectile so that simulated positional forces might be measured with fixed equipment. Lack of complete simulation made it necessary, however, to develop and apply a correlation factor to the idealized theory of Ref. 1 so that meaningful comparisons could be made with the experimental results. Once this is done, theory and experiment agree quite well.

In the other set of experiments, the objective was to simulate the conditions under which the projectile experiences lateral damping forces, i.e., that component of the guidance force that tends to retard or damp lateral motion to achieve stability. In conjunction with guideway damping elements, these forces are generated electrodynamically as a result of the lateral motion itself. It has been possible to simulate the conditions with a pendulum and a short section of simulated guideway. Damping forces have been inferred from the rate at which oscillations of the pendulum decay. The experimental results thus obtained agree well with Ref. 1 theory.

2.0 REVIEW OF THE CONCEPT

The general overall arrangement of the system concept is shown in Fig. 1. The guideway is provided by four, range-length line currents of magnitude I_D and four, range-length sets of transposed line current segments of length (ℓ) and magnitude (I_P); all of which are symmetrically orientated about the range centerline. Also, the projectile is a flared cylinder with a conductive shell around the cylindrical portion. The nose piece to be tested is optional.

7

The pattern of the guideway's magnetic field produced by the I_D currents alone is shown in Fig. 2. A similar so-called null-flux field is produced by the I_P currents alone except that the flux is of opposite direction in adjoining segments. Because I_D is greater than I_P, the resultant field of all the currents is a range-length null-flux field that is modulated with respect to distance downrange. Thanks to the principle of superposition, however, that part contributed by I_D and that part contributed by I_P can be considered independently insofar as interaction with the projectile is concerned. For consideration of either, an important point that should be stressed is that the field is strong near the currents and decreases to zero or the null value at their axis of symmetry; i.e., the guideway axis which coincides with the range centerline.

Now visualize the projectile to be in high-speed downrange motion parallel to the guideway axis. It will experience no change in the field of the I_D currents so that no electrodynamic interaction with them will occur. However, as it passes from segment to segment, there is exposure at relatively high frequency to a field of opposite polarity insofar as the I_P currents are concerned. At each change in polarity, the intent is that the induced voltages eliminate an existing set of eddy currents in the conductive shell and create ones of opposite direction that will persist until the next change. From Lenz' law, the field of the eddy currents is in direct opposition to, and tends to cancel or nullify, the change which caused them. Hence, the shell tends to appear as a diamagnetic object in the field of the I_P currents. To the extent this is achieved, the shell is repulsed by these currents and causes it to seek a position of equilibrium in the null-flux region along the guideway axis. Because these forces and their resultant depend on the shell's lateral position with respect to this axis, they are called magnetic positional forces and are denoted by F_M as in Ref. 1. Correspondingly, the I_P currents can be considered as the positional force elements of the guideway.

Also, consider that there is a relatively slow lateral motion of the projectile as it progresses downrange. The timewise average of the added electrodynamic forces acting on the projectile are of interest to produce stability. To determine this average, it is necessary to consider only the average magnetic field, which is the field of the I_D currents. As can be seen from Fig. 2, lateral motion in this field results in the projectile's exposure to changing flux so that again eddy currents are induced in the conductive shell. However, as stated above, lateral motion is slow so that the eddy current energy is dissipated in the shell as joulean heat at the same rate it is generated. Therefore, the lateral motion generating the currents is retarded or damped. Hence, the I_D currents can be considered as guideway damping elements that apply a damping force (F_{MD}) to the projectile (Ref. 1).

As indicated in Fig. 3, F_M and F_{MD} effectively act on the projectile through a magnetic force center (c_M) that is a distance (ℓ_M) forward of its center of gravity (c_g).

Also, for stability purposes, the aerodynamic forces act through an effective center of pressure (c_p) at a distance (ℓ) aft of c_g. At any time the projectile is off course, F_M forces its nose toward the guideway axis. A change in angle of attack is then to enlist aerodynamic forces to aid in correction of the course. Once this corrective action is underway, F_{MD} is effective in reducing overshoot and damping oscillations about the guideway axis.

3.0 POSITIONAL FORCE EXPERIMENTS

3.1 APPARATUS

The apparatus designed and built for this set of experiments is illustrated in Fig. 4. From a mechanical viewpoint, it consists essentially of a large diameter coil containment wheel that has a safety brake and is rotated by a variable-speed drive unit. From an electrical viewpoint, it consists of an I_P simulation coil, a 0- to 1,000-amp variable d-c power supply and slip rings for energization of the coil, and models of projectile conductive shells. As indicated, the coil is contained by, and moves with, the rim of the wheel while the model is fixed on a multi-component wind tunnel force balance. The balance in turn is mounted on a stationary cross-feed that has a vernier for model positioning.

The geometry of the coil itself is shown in Fig. 5. It consists of five layers or turns and provides two zigzag patterns of current flow in opposite directions around the inside diameter of the wheel rim. Alternate segments of the zigzag patterns, shaded in the sketch, form a circle around the rim's axial center, and it is these portions of the pattern that are intended to simulate I_P segments of the guideway. The unshaded portions of the patterns ideally would be sufficiently remote from the model to be ineffective in generating forces. The extent to which this has not been achieved, however (see Fig. 6), is believed to be fair compensation for the fact that there is effectively a significant space between adjoining segments of interest (in addition to insulation space between segments, there is a tendency for currents to take shortcuts around corners at their ends).

The overall idealized scheme, which the apparatus attempts to emulate, is illustrated in Fig. 7. Ideally, I_P elements would be made to travel in a circle, and each element should exist to the next element. The cylindrical shell would then be positioned a distance (r_1) from the circle and have an axial curvature to match. With various rotational speeds, the electrodynamic forces acting on the cylinder would then be measured. These would include the force of repulsion (F_M), the drag force (F_{DRG}), and the moment about the point of measurement. With a circle of sufficient size, the interaction should approach that which would occur between the conductive shell on a projectile and one co-linear set of line current segments. The results for four such sets in a null-flux configuration would be obtained by superposition.

For the present experiments, which utilize currents that are distributed over the finite cross-sectional area of five turns, an equivalent filamentary current (I_P) is assumed to be at the geometric center of this area. Its effective magnitude is the total current in the five-series turns; i.e., $I_P = 5\,I_s$ where I_s is the power supply current.

The three cylindrical shell models, which were utilized in the experiments, are shown in Fig. 8. They are identical except for having individual lengths of 0.0508, 0.1016, and 0.1524 m, respectively. All are made of OFHC® copper, have an outside diameter of 0.0508 m, and a wall thickness of 0.00254 m except for the end closures which are 0.00635-m thick. Their curvature of axis is intended to match the curvature of the rotating coil.

A printer-scanner and an integrating digital voltmeter were provided for recording the experimental data in digital form. Items recorded included the rotational speed of the wheel as sensed with a tachometer, the current I_s as measured using a current shunt, the force balance outputs, and the excitation voltage to the strain-gage bridges of the balance.

3.2 PROCEDURE

Before measuring the forces on each of the three models, a careful test stand alignment of the shell with the force balance components was made, and they in turn were aligned with the Earth's vertical and horizontal. The balance was then calibrated against weights of known value.

With the model remaining fixed to the balance, the two were subsequently moved to the rotating apparatus where care was taken in attaching the balance to the cross-feed to maintain vertical and horizontal orientation. The cross-feed was then raised or lowered to provide best alignment between the model contour and the coil. A chosen reference distance (r_1) between the shell axis and the coil center was then carefully established, and a corresponding reference reading on the cross-feed vernier was recorded.

To begin the simulation and measurement of forces, a desired rotational speed was first established, and the model was positioned at a desired r_1 through appropriate setting of the cross-feed vernier. Finally, with zero conditions being recorded, both before and after, the I_P coil was energized for a period of 30 sec, during which force measurements were made. The coil was then allowed to continue rotating while cooling for a period of five minutes prior to the next data point. The process was continued until a grid of data was obtained for speeds from 250 to 1,750 rpm and for values of r_1 from 0.037 to 0.072 m. During the process, some additional data were taken with the model of medium length to determine the effect of misalignment between model and coil.

Finally, to enable a more accurate determination of r_1 under actual test conditions, it was necessary to measure the containment wheel growth versus speed and the force balance deflection versus force. As might be expected, the wheel growth was found to be proportional to the square of its rotational speed, and the balance deflection proved to be a linear function of the applied forces.

3.3 RESULTS AND DISCUSSION

The Ref. 1 theory, which the experimental results are intended to validate, predicts that in an idealized experiment the force of repulsion per unit length on the conductive shell should be

$$F_r = \frac{\mu_o I_p^2 a^2 (\delta - 1)}{2\pi r_1 (r_1^2 - a)} \tag{1}$$

where

    μ_o is the permeability of free space

    I_p is the simulated guideway current

    a is the effective shell radius

    r_1 is the distance from I_p to the shell axis

and where δ is the ratio of the magnetic field within the cylinder to that which would exist at the same location if the cylinder were absent. Reference 1 gives its value as

$$\delta = \sin \left\{ \tan^{-1} \left[\frac{-2\varsigma}{\omega\mu_o a} \right] \right\} \tag{2}$$

where ς is the area resistivity of the shell and ω is the angular velocity at which it is exposed to a field of alternate polarity by the passing I_p elements.

Unfortunately, certain compromises had to be made in design of the apparatus so that the actual experiments have been somewhat less than ideal. As is seen from Eq. (1), it is desired that δ be small so that F_r will be large. From Eq. (2) then, ς must be small, or the product of ω and a must be large. In fact, however, the radius (a) had to be limited to a relatively small value to match the size of the rotating apparatus. It, in turn, was limited in size by availability of resources. Because the choice was made

to avoid cryogenics, the effective ς was limited to the relatively large values which could be obtained at room temperature with OFHC copper and a shell thickness to match a. Thus forced toward large values for ω and limited to relatively low peripheral velocities achievable with rotating machinery, a small segment length (ω) was necessary for the experimental I_P. This compromise is considerably less severe in an actual range where projectile velocities are 4,000 to 6,000 m/sec.

When compared with all radial guideway and projectile dimensions, Ref. 1 theory presumes that ω can be at least 20 times greater and thus treats segments as being infinite in deriving theory. The implications of ω not being so great was made clear by computing the ratio (B_{TRP}/B_{INF}) as a function of z' for various values of ω/r' where B_{TRP} is the field that would exist a distance (r') from a co-linear set of transposed segments of length (ω) and where B_{INF} represents that field which would exist if the set were replaced by an infinite line current. A plot of the computed results (Fig. 9) shows that the average field intensity, to which a conductive shell is exposed, is weak for $\omega/r' \leqslant 5$ as was the case in the present experimental situation. It is, therefore, necessary to develop and apply a correlation factor ($f_{corr}(\omega, a, r_1)$) to the Ref. 1 theory for meaningful comparisons to be made with the experimental results. The derivation of expressions for this factor is given in Appendix A, which includes a computer program for evaluation under specific conditions.

The actual experimental results for F_r together with Ref. 1 theory and Ref. 1 theory times $f_{corr}(\omega, a, r_1)$, as the latter applies to the experimental situation, is shown in Figs. 10a through h. The data show that there is no consistently discernible difference in the results for the three different h/a ratios tested. This is as it should be since F_r is force per unit length. However, with thick end closures, the h/a ratio is not required to be excessively great for two-dimensional mathematical modeling to be satisfactory.

The data are considerably below predictions of the idealized Ref. 1 theory, especially at increasing values of r_1/a. The percentage of disagreement is considerably less at small r_1/a, as was expected. The application of $f_{corr}(\omega, a, r_1)$ to the theory brings it into harmony with the data at the larger values of r_1/a, but overcompensates at the smaller values of this ratio. One explanation of this is that the effective location of I_P is closer to the shell than was assumed; i.e., the effective r_1 may be less. If it is considered that geometric mean distances are normally used to quantitate the mutual inductance between conductors, this explanation is quite plausible (Ref. 2).

Another possible reason for the discrepancy is that the effective value of a = 0.02413 m which was used to correlate the data was not the proper choice. This was based on the distance from the shell axis to the midpoint of its wall. Use of a = 0.0254 m (the

radius of the outside surface) would have resulted in better agreement. Neither explanation will be pursued, however, as the agreement shown is good considering the compromises in both theoretical derivations and experimental design. Agreement is adequate for rotational speeds of the apparatus from 250 to 1,750 rpm where theoretical values of S from 0.67 to 0.13 were attained.

In addition to confidence in predicting values for F_r, it is important that its value be large with respect to the corresponding drag force (F_{DRG}). Therefore, experimentally measured values of F_{DRG} have been utilized in conjunction with the experimental values of F_r to formulate the ratio (F_r/F_{DRG}). The results for the three shell models at four different r_1/a positions are plotted in Figs. 11a through c and 12a through c, inclusively. From these, it is clear that, as the correlation parameter (μ_o a $\omega/2 \varsigma$) (see Eq. (2)) is made small, F_{DRG} becomes a significant factor, whereas it becomes insignificant as compared with F_r when this parameter is made large. This trend was predicted in Ref. 1 based on the fact that, for low values of the parameter, the eddy currents in the shell are dissipated at the rate they are induced, whereas, for high values they tend to be persistent and result in shielding. From Figs. 11a through c alone, it is also clear that the magnitude of F_{DRG} slightly increases with decreasing values of the shell's h/a ratio. While not serious for anticipated values of h/a, this trend is to be expected from the increasing importance of end effects. Similarly from Figs. 12a through c alone, it is clear that the magnitude of F_{DRG} also increases slightly with increasing values of the r_1/a ratio. In this case, the trend can be attributed to the fact that, at larger r_1/a, the inducing field and the eddy current field become less two-dimensional so that the eddy current pattern is more circular. If ϑ were larger as would be the case in an actual guideway, this trend would not be expected.

Equally important to the magnitudes of the forces is the establishment of a point on the shell through which they can be assumed to act. To resolve this, the moment was measured each time, about the same point at which F_r and F_{DRG} were being sensed. For convenience, the authors have chosen to use this measured moment to transfer F_r and F_{DRG} to an effective point of action that lies on the shell axis at a distance ($\Delta \ell_M$) aft of the shell's geometric center. In this way, although the moment is essentially a result of F_{DRG} being off axis, its effect can be accounted for by a change ($\Delta \ell_M$) in a guided projectile's magnetic moment arm (ℓ_M). It so happens that the experimental results collapse to a simple function of the correlation parameter (μ_o a $\dot\omega/2 \varsigma$) as shown in Fig. 13. At larger values of this parameter where a guideway system would operate, the magnitude of ($\Delta \ell_M$) decreases.

A final set of positional force data was taken to determine the effects of misalignment between the shell axis and I_P, as might be expected in the case of a projectile in a guideway. This was done at a relatively large fixed value of the correlation parameter and at a fixed r_1/a ratio with the angle included between I_P and the shell axis being varied up to 10 deg. The results for F_r and F_{DRG} versus the angle are shown in Fig. 14, where it can be seen that they are little perturbed. However, there is a significant effect insofar as their effective location is concerned as illustrated in Fig. 15 where $\Delta \ell_M/a$ is plotted versus the angle. Care must, therefore, be taken when designing actual projectiles for guidance to ensure that ℓ_M/a is sufficiently large and that the included angle between a projectile axis and the guideway axis does not assume excessive values during flight.

4.0 DAMPING EXPERIMENTS

4.1 APPARATUS

Since electromagnetic damping of a projectile's lateral motion is a consequence of only that component of motion which is normal to the guideway axis, it was possible to devise an experimental apparatus closely simulating the necessary conditions of an actual system. The apparatus consisted essentially of a pendulum whereby a cylindrical copper shell or model with closed ends resembling the conductive portion of the guided projectile in Ref. 1 was suspended in a null-flux field of four simulated I_D currents (see Figs. 1 and 2). Figure 16 shows a cross section of the apparatus, and Fig. 17 is a photograph of the actual hardware.

The I_D currents were simulated by a coil of nine turns of copper tubing wound on a wooden form. Since the power supply provided a maximum of only 1,000 amp, a nine-turn arrangement was used to increase the effective I_D and the resulting null-flux field for greater damping, i.e., $I_D = 9\ I_s$. To reduce possible end effects of the coil, its length was made significantly longer than its radial dimension (b); a 1.2-m length was used with the effective b dimension of 0.0898 m. Since a maximum energy dissipation rate of approximately 65,000 w was required, water cooling was employed.

Four different shell models (Fig. 18) were used to investigate the effects of different parameters. All had an outside diameter of 0.0254 m; two were 0.005 m and two were 0.01 m long. One of each length had a wall thickness of 6.35×10^{-4} m, and one of each length had a wall thickness of 1.245×10^{-3} m. All had 4.775×10^{-3}-m-thick copper end closures attached with silver solder.

The cylindrical shells were drilled through at their midpoints and were attached to threaded stainless steel rods with brass nuts (in an attempt to have no ferromagnetic materials involved). These assemblies then had razor blades secured to their other ends

(see Fig. 16) to provide low friction pivots when placed in the grooved fixture on the stand holding the I_D coil.

The apparatus was designed to allow adjustment of the model's position in the null-flux field and, thereby, acquire damping data at various locations.

Data were taken using a prototype laser vibrometer (Ref. 3). Use of this instrument allowed continual non-interference monitoring of the model's position and velocity. The models were equipped with retroreflectors (corner reflectors), and the instrument was located approximately one meter from the pendulum. Data output was in the form of strip charts (see Fig. 19 for a typical example).

4.2 PROCEDURE

The procedure was to place each model at some selected (and known) location in the field, then to displace it slightly, release it, and observe its decaying oscillatory motion. Adjustments on the stand were used to shift the pendulum either horizontally or vertically. A piece of clear cellophane with grid markings was mounted near one end of the pendulum to facilitate locating the models at the desired positions. Data were then taken for the various models at numerous positions using different current levels. Data were also taken with no current to determine damping due to factors other than the magnetic field.

Current level in the coil was determined from its terminal voltage after having used a Kelvin bridge to determine its resistance. Coil temperature was monitored with thermocouples and a digital meter.

After experiments had been completed with the coil situated as shown in Fig. 16, the coil was rotated approximately 22.5 deg about its indicated pivot, and data were taken at numerous locations in the rotated field. This was done to enable measurement of purely radial and purely angular damping coefficients for an angular position, or β, other than $3\pi/4$ and $\pi/4$, respectively.

4.3 RESULTS AND DISCUSSION

In the experimental setup, the various dimensions were of the same order of magnitude as in the proposed system (Ref. 1). However, there were some quantities which differed appreciably from what would be expected in an actual guidance system. The I_D current levels, despite the effect of having a nine-turn arrangement, were significantly lower than the 100,000 amp used in Ref. 1. The lateral velocity of the models in the experiments was also significantly different from that anticipated during guided flight. These differences amounted to approximately two orders of magnitude in the case of the current level and

several orders in the case of lateral velocity. However, damping forces were generated which were adequate for measurement and correlation.

The intent of the experiments was primarly to verify magnitudes of the damping coefficient (K_{MD}) in the central region of the field where $\Re/b \leq 0.3$, and to verify trends in that coefficient in the region where $\Re/b > 0.3$. Because theory predicted that the damping was nearly uniform in the region where $\Re/b \leq 0.3$, the guidance system relied on restricting flight to that region and using a constant value for K_{MD}. It was, therefore, important that this constant be confirmed. It is also interesting to observe how well theory and experiment agreed in the outer region where $\Re/b > 0.3$. In addition to the inaccuracies of the simulation already emphasized, filamentary currents were assumed in the theoretical treatment, whereas nine turns of 0.008-m-diam copper tubing were used in the experiment. There was the possibility that the assumed b was not accurate since the copper tubing was somewhat difficult to position on the form and rather bulky insulating material was used between the conductors. These experimental inaccuracies were presumed to have a more dramatic effect as $\Re/b$ increased, and therefore, some error was to be expected in the outer region.

Experimental results took the form of strip charts, (see Fig. 19). Data retrieved from these charts consisted of the magnitudes of the quantities identified as $2X_1$, $2X_2$, and Δt. As explained in Appendix B (Eq. (B-5)), these are adequate for extraction of K_{MD} from the relationship

$$K_{MD} = \frac{\ell}{\ell_M} \left\{ \frac{2M}{\Delta t} \ell n \frac{X_1}{X_2} - C_D \right\} \tag{3}$$

where

$\qquad C_D$ = Damping due to factors other than magnetic field (Eq.(B-6))

$\qquad M$ = Mass of pendulum

$\qquad \ell$ = Separation between the pendulum's pivot point and the center of gravity.

and $\qquad \ell_M$ = Separation between pivot point and center of magnetic forces

According to Ref. 1 theory, it should then be possible to present the results in normalized form by plotting $K_{MD} b \ \varsigma/(hI^2)$ versus $\Re/b$ for each β. For this reason, numerous measurements were performed prior to the actual tests. A summary of the measurements is tabulated below for use as needed. Other measured quantities not shown include a chart speed of 2.52×10^{-3} m/sec and a coil resistance of 6.58×10^{-2} ohm.

I_s currents from 400 to 700 amp were used. This provided, since nine turns were used, a magnetic field equivalent to one produced by a filament carrying from 3,600 to 6,300 amp.

No.	Shell Length, h, m x 10^3	Shell Wall, w*, m x 10^4	Shell Radius, a**, m x 10^2	Area Resistivity, ς***, ohm x 10^5	Coil Bore, b, m x 10^2	Pendulum length, ℓ, m x 10	Pendulum length, ℓ_{η}, m x 10	Pendulum Mass, M, Kg x 10^2
1	5.0	6.35	1.24	6.563	8.98	2.643	3.088	8.84
2	5.0	12.446	1.21	2.427		2.719	3.119	10.49
3	10.0	6.35	1.24	6.563		2.635	3.088	8.69
4	10.0	12.446	1.21	2.427		2.762	3.119	11.96

* Side wall only; end walls were 4.775×10^{-3} m for all models

** Radius based on wall midpoint

*** Based on measured end-to-end resistance of long models which was 3.25×10^{-5} and 8.57×10^{-5} ohm for thick and thin shell, respectively.

During the experiments, it was found that the stainless steel pendulum rod appeared to be slightly ferromagnetic. This caused some displacement of the pendulum's equilibrium position in part of the experiments. The displacement was determined from the strip charts, and corrections for equilibrium position were included in the results to be presented.

Theory developed in Ref. 1 indicated that the damping coefficients arising from radial motion or from angular motion should be identical. It was convenient to simulate purely radial and purely angular motion relative to the axis of the null-flux field at only certain angular positions because of interference between the coil and pendulum. Note in Fig. 16 that, at points where the pendulum's motion is at right angles to a radius from the coil axis through the equilibrium position of the pendulum, the motion is angular, while that motion on a path coinciding with a radius is radial. Figures 20a through c present experimental results and theoretical predictions for damping coefficients resulting from the damping of radial motion, whereas Figs. 21a through c depict results arising from the damping of angular motion. The results shown in Fig. 20a were obtained with the thick shell model with β (see Fig. 16) equal to $\pi/8$ and with $\Re$ varying from 0 to 0.5 b. As the captions indicate, Figs. 20b and c and 21a through c are for a variety of situations with different shells, locations, and directions of motion. Examination of these figures reveals satisfactory agreement between experimental and theoretical results and confirms that the damping coefficient is insensitive to whether the direction of motion is radial or angular.

Since theory and experiment suggested that the damping coefficient is independent of direction of motion and since the experimental apparatus was more conducive to obtaining results at points where motion of the pendulum was not purely radial or angular, numerous results were obtained for situations where motion was a combination of radial and angular. Figures 22a through h show the resulting combination damping coefficients for the different shell models and positions. These figures include the theoretical predictions for damping coefficients obtained, assuming either radial or angular motion, and provide confirmation that direction of motion is not an influencing factor on damping. Satisfactory agreement is also revealed between theory and experiment where $\Re/b$ is small and trends are shown to be as expected for the larger values.

It is noticeable that experimental damping coefficients for the thin wall models are consistently larger than those for the thicker wall models. This is reasonable since the theory does not take into account eddy current losses in the rather thick end plates. It is to be expected that these losses would be a significantly greater percentage of the total in the thin models as compared to the thick ones. The influence of the end plates is more evident in the short model data which are included in Figs. 20b, 20c, 21b, and 21c. It is in the case of the thin short models that the effect is most pronounced.

Reference 1 assumed that, since any deviation of the model's axis from parallel to the guideway axis would be small, the effect on damping coefficients would be minor and could be neglected. This assumption was experimentally verified as shown in Fig. 23. The results are presented as ratios of misaligned versus aligned damping coefficients. Shell models were misaligned as much as 14 deg with no noticeable effect on damping coefficients.

5.0 CONCLUDING REMARKS

As shown in Ref. 1, the determination of the feasibility of an electromagnetic-guideway/guided-projectile system was dependent on the use of theoretically derived magnetic force coefficients. The purpose of the experimental program described herein was to validate those coefficients. Two sets of experiments were used to simulate positional and damping forces as would be generated in the actual guidance system. These were, in turn, used to find force coefficients for comparison with those predicted using techniques developed in Ref. 1.

The experimental apparatus used for generating positional forces had much shorter "positional" current segments than proposed for the actual system. This necessitated developing and utilizing a correlative factor when comparing the theoretical predictions from Ref. 1 with experimental results. The comparison clearly indicated the validity of the analytical techniques, substantiating both trends and magnitudes.

In the case of the damping experiments, the apparatus closely resembled the proposed system and no corrections were indicated. Results were in close agreement with theory and very satisfactorily corroborated the accuracy of the previously developed theory.

REFERENCES

1. Arney, G. D., Jr. and Pender, C. W., Jr. "A Magnetic-Guideway/Guided-Projectile System Concept for Aeroballistic Ranges." AEDC-TR-76-149, February 1977.

2. Grover, F. W. Inductance Calculations. D. Van Nostrand Company, Inc., New York, 1946.

3. Bomar, B. W., Goethert, W. H., Belz, R. A., and Bentley, H. T., III. "The Development of a Displacement Interferometer for Model Deflection Measurements." AEDC-TR-76-116, January 1977.

4. Corson, D. R. and Lorrain, P. Introduction to Electromagnetic Fields and Waves. W. H. Freeman and Company, San Francisco, 1962.
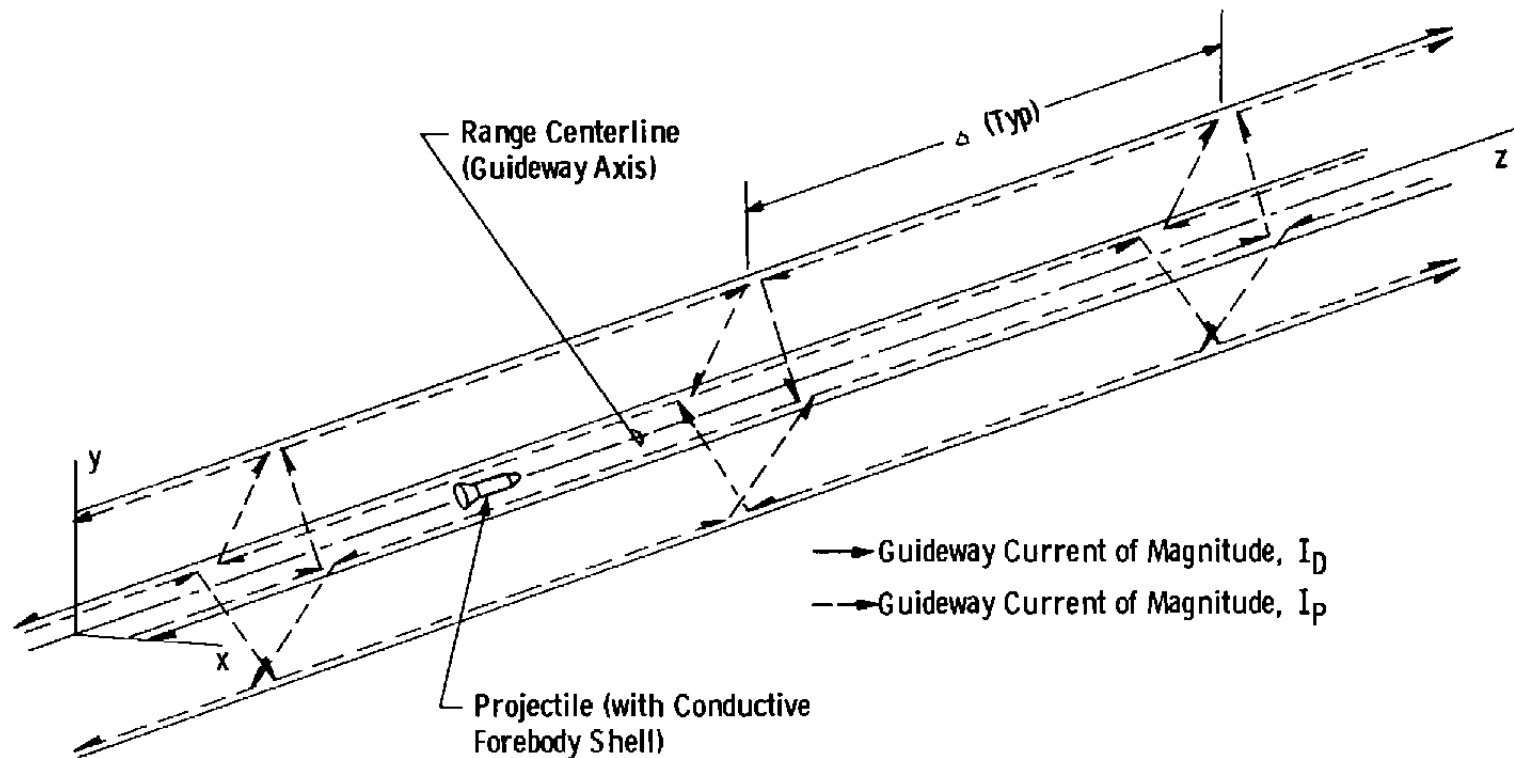
Figure 1. System concept.

Figure 2. Null-flux field.

Optional Nose
or Test Article

Conductive Cylindrical Shell

ℓ_M

ℓ

α

$\overline{V}$

c_M

γ

Lift

c_g

z

Drag

c_p

y

Non-Conductive Material
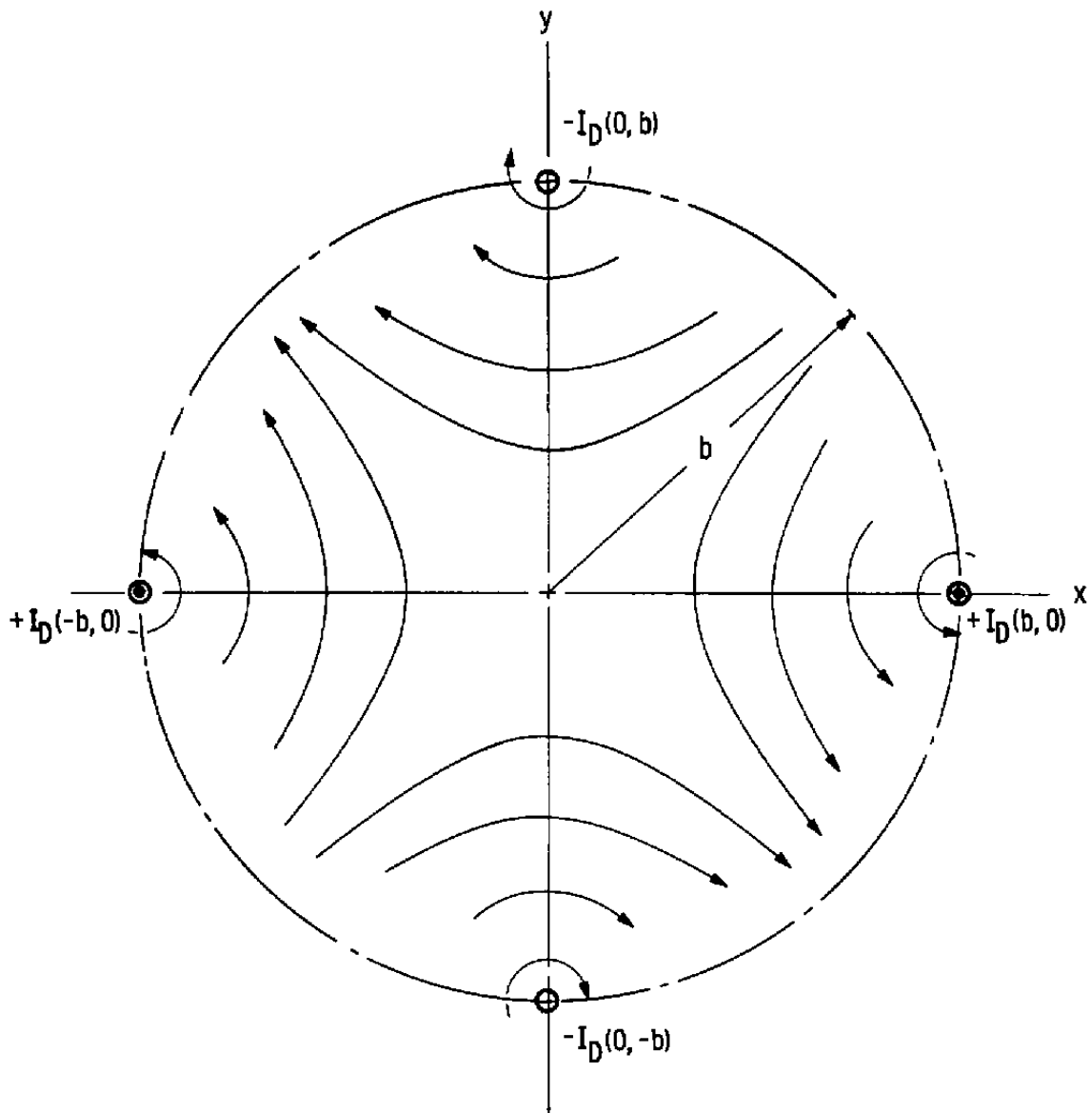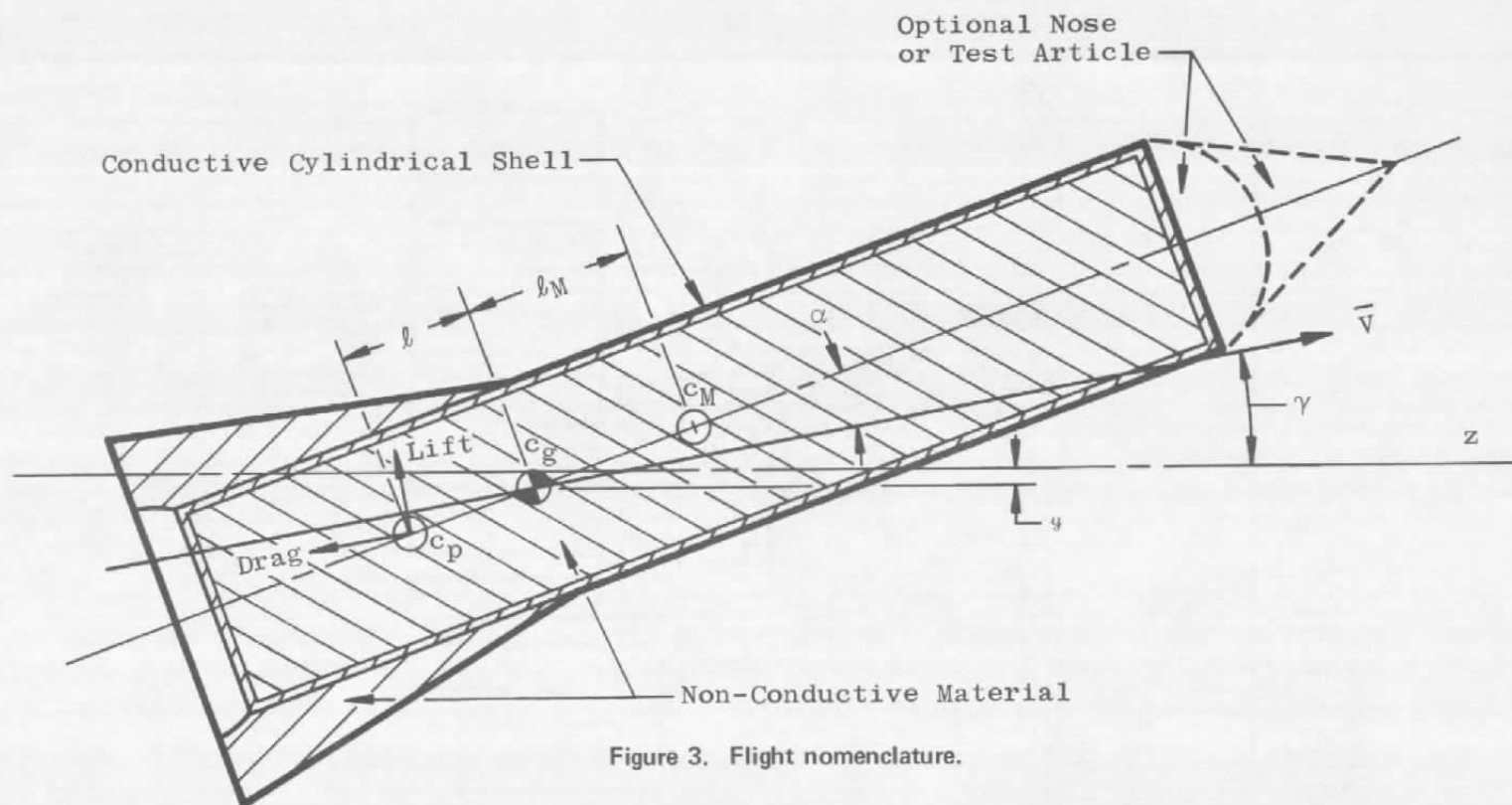
Figure 3. Flight nomenclature.
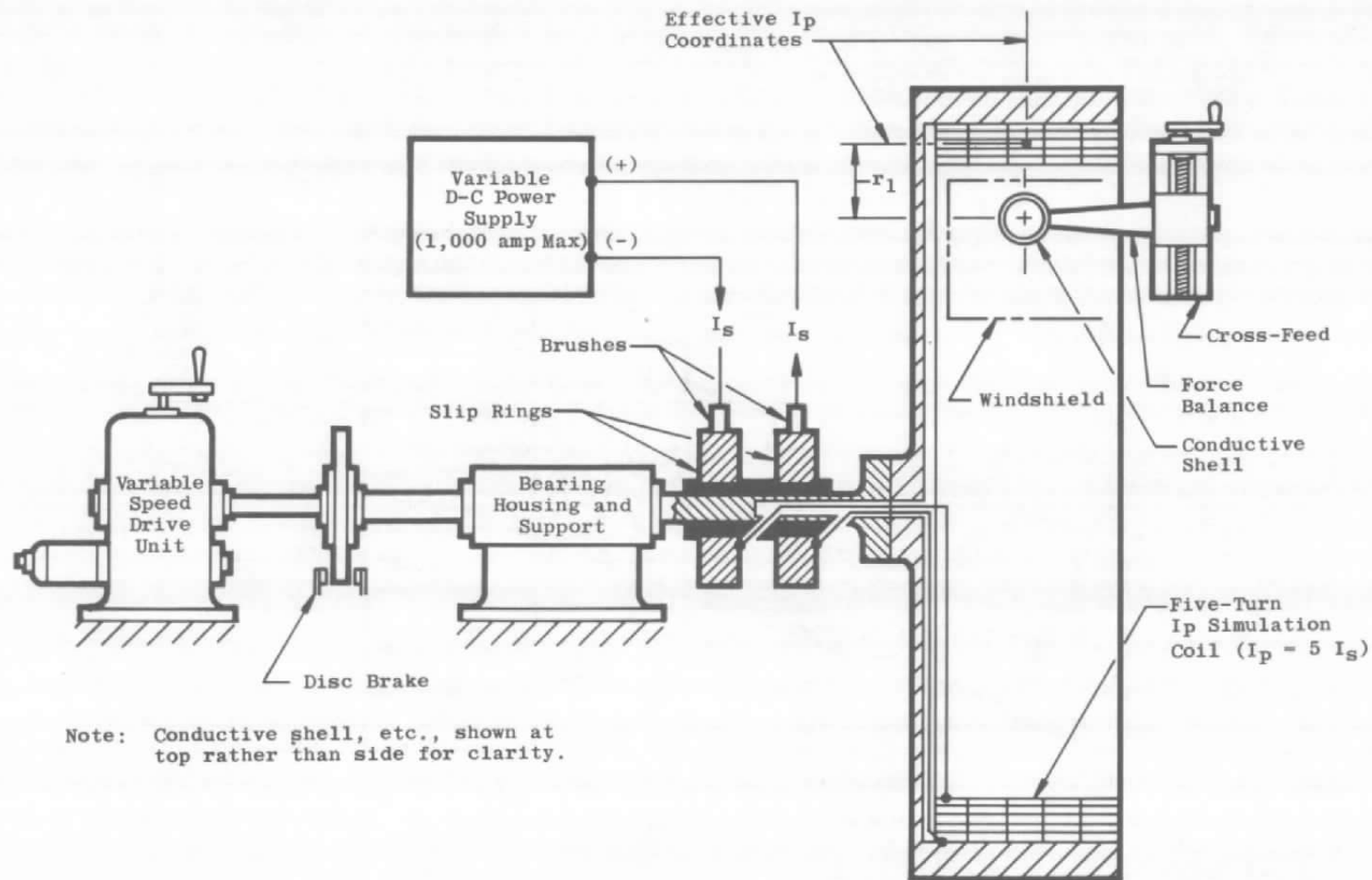
Figure 4. Sketch of positional force apparatus.
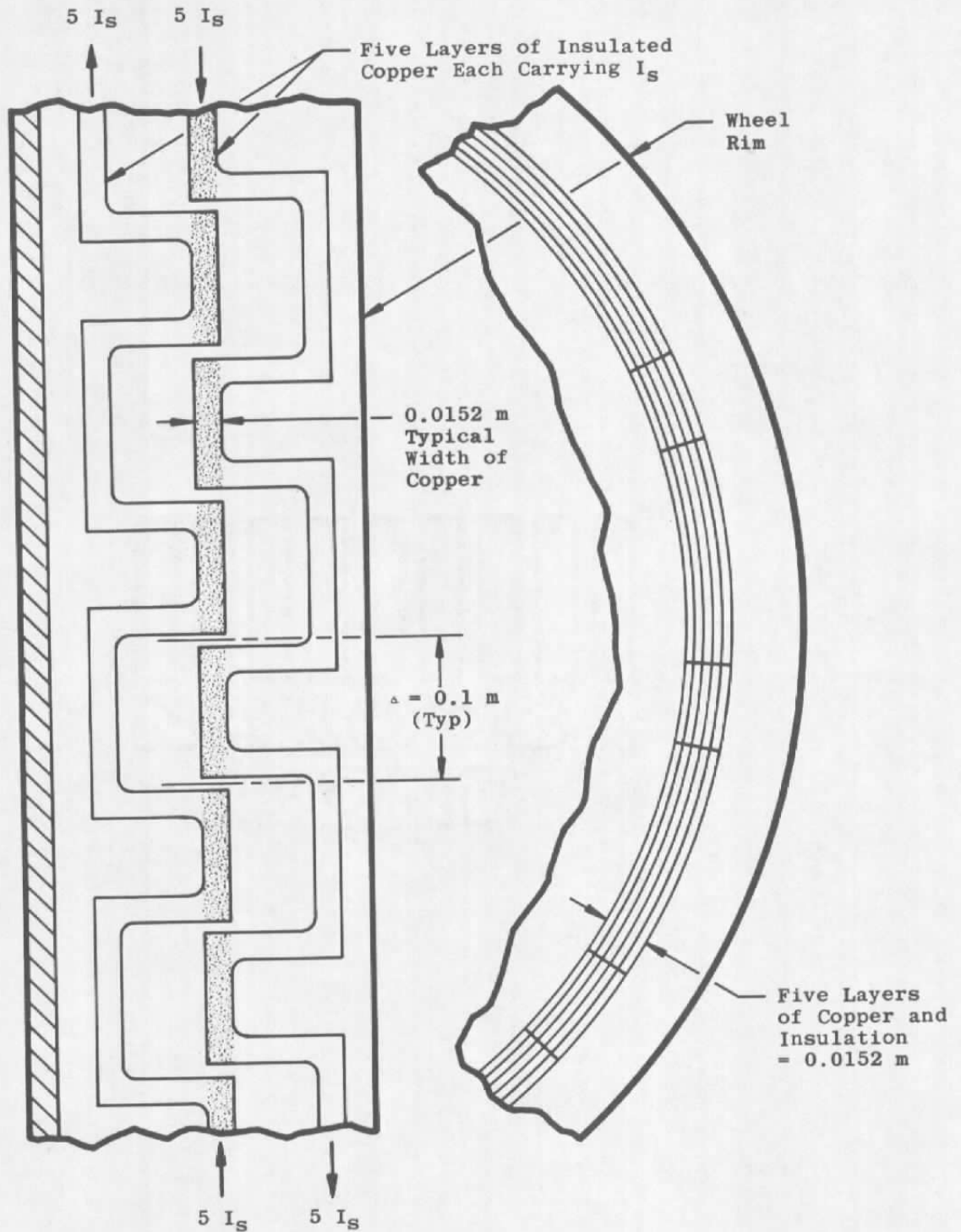
Figure 5. I_p coil geometry.

Note: Windshield Removed for Clarity

Drive Unit

Cage for
Brake and
Slip Rings

Force Balance and Cross-Feed

Model

Ip Coil

A E D C
5445-76

Containment Wheel
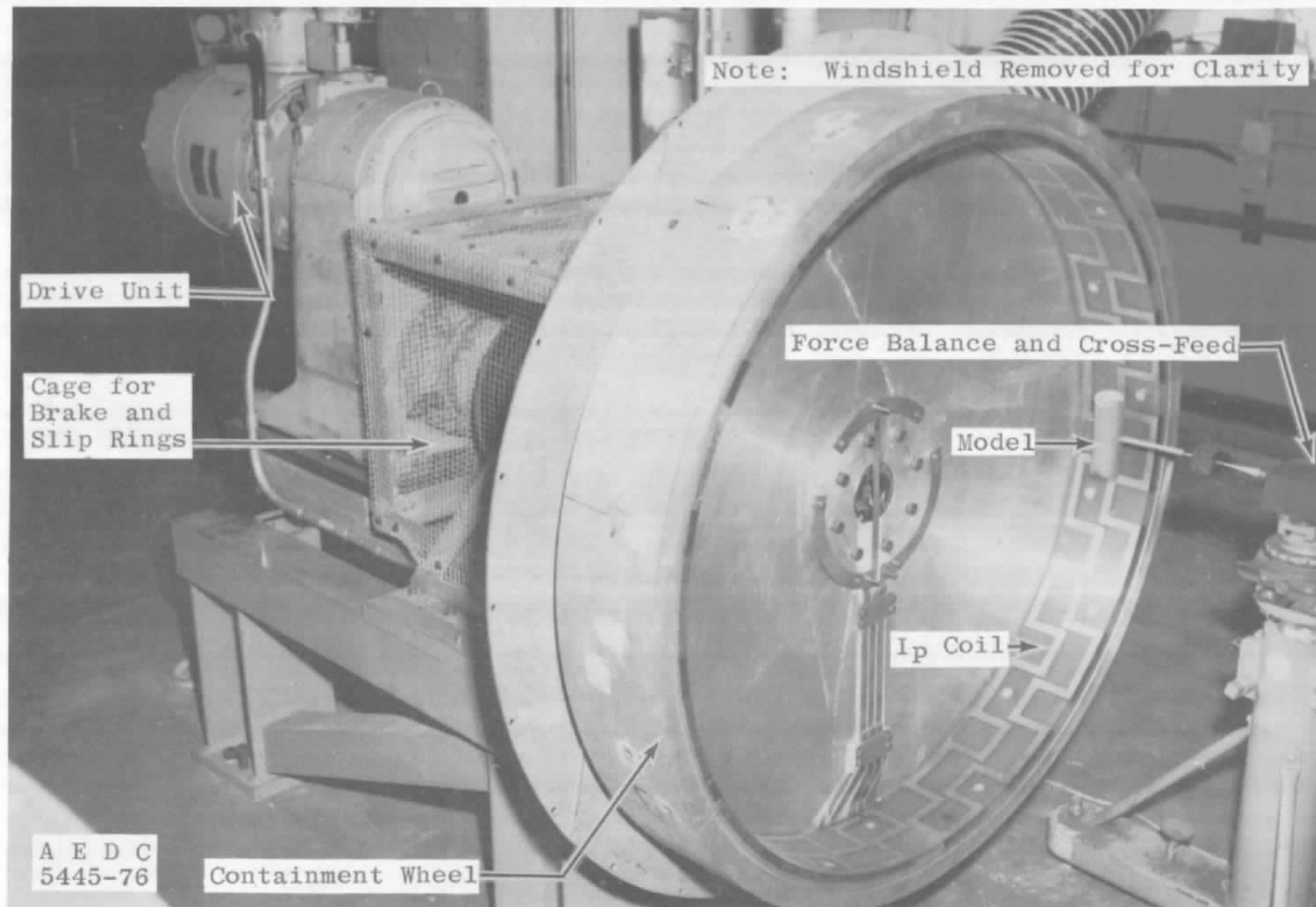
Figure 6. Photograph of positional force apparatus.
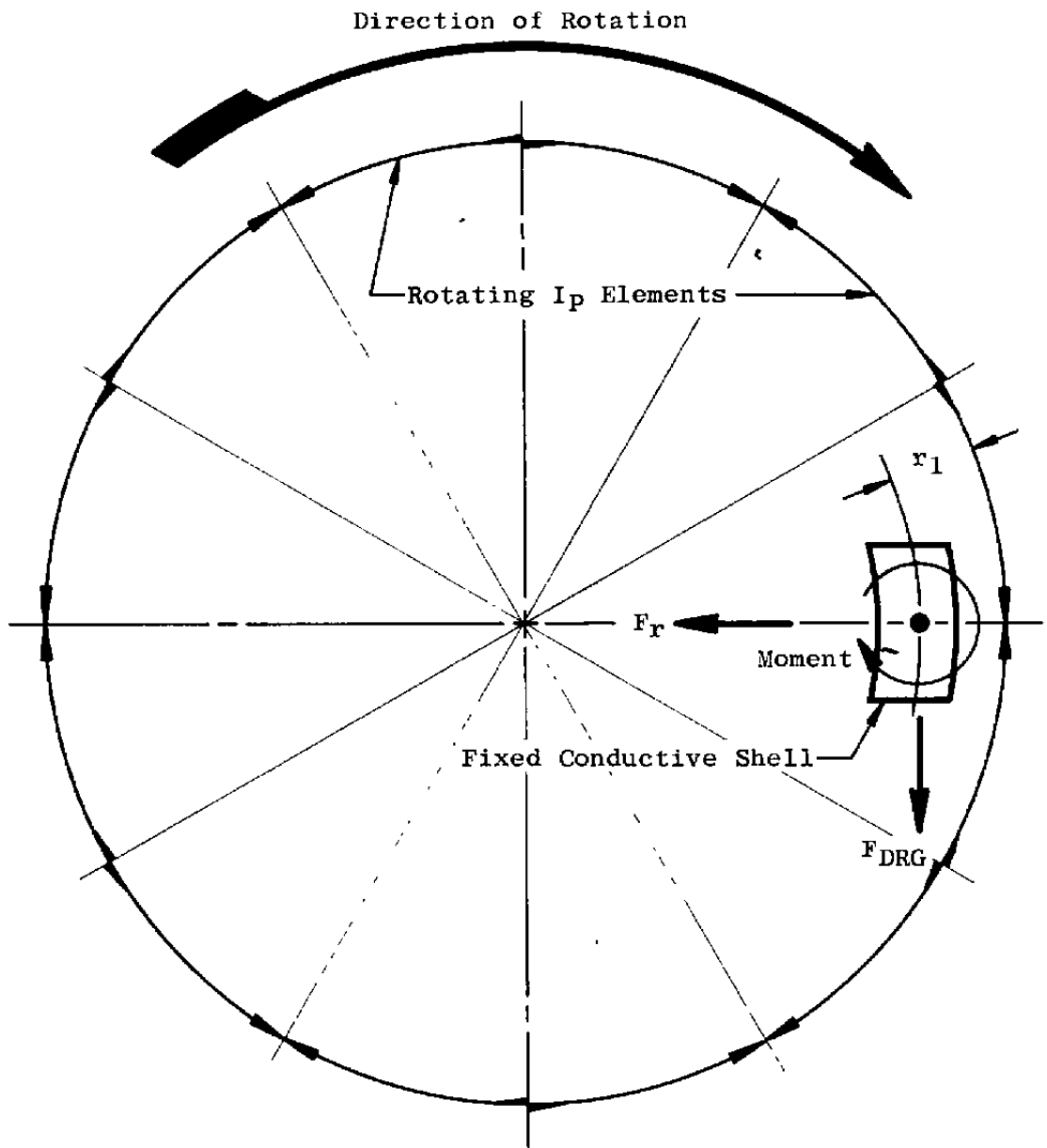
Figure 7. Scheme of positional force apparatus.
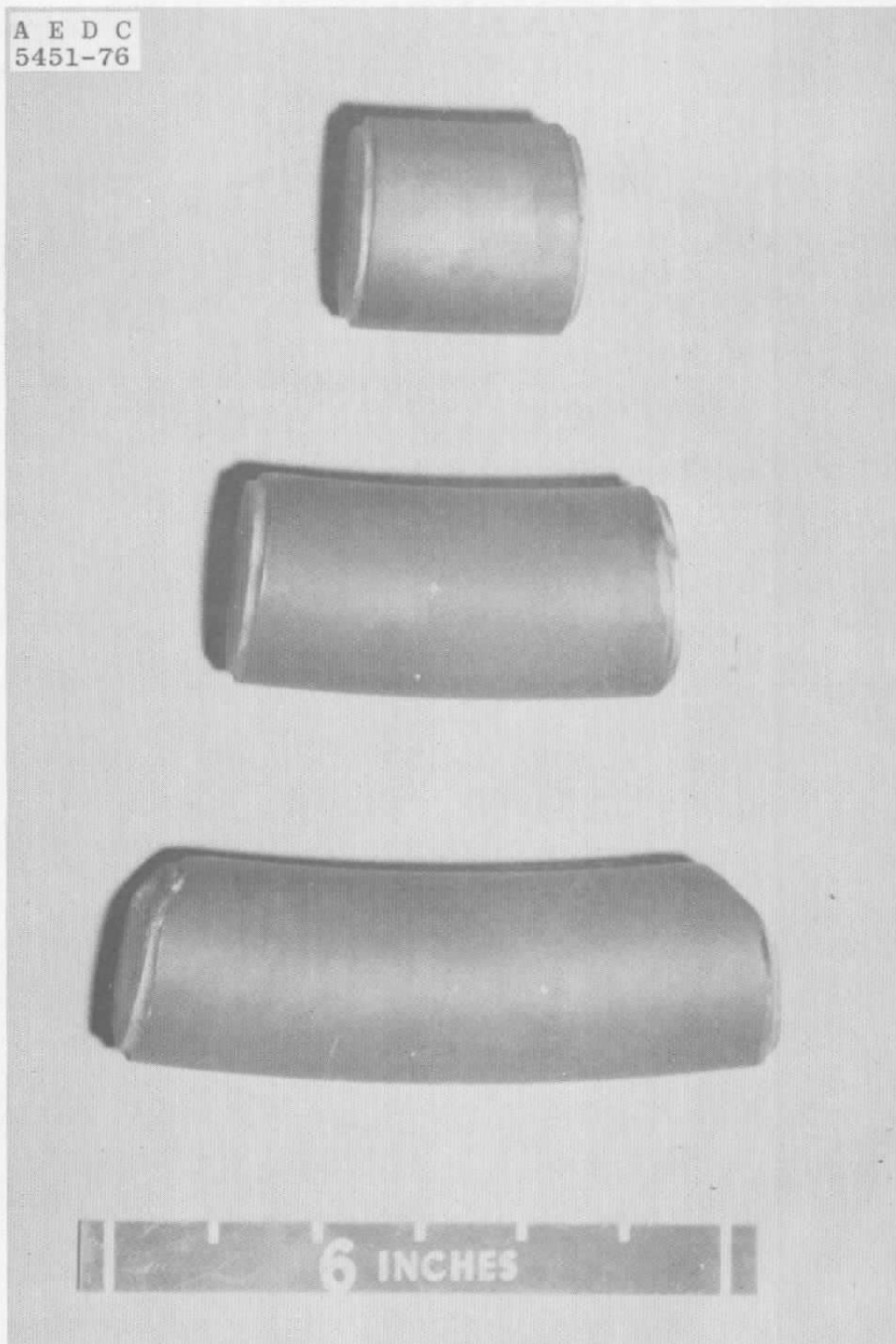
Figure 8. Photograph of conductive shells for positional forces.

$\Delta/r' = 20$

$\Delta/r' = 5$

$\Delta/r' = 25$

1.0

$\Delta/r' = 15$

0.8

$\Delta/r' = 10$

$\left|\dfrac{B_{TRP}}{B_{INF}}\right|$ 0.6

$\Delta/r' = 3$

0.4

$\Delta/r' = 2$

0.2

$\Delta/r' = 1$

0

$\dfrac{n-1}{2}\Delta$ $\dfrac{n+1}{2}\Delta$ $\dfrac{n+3}{2}\Delta$ z'
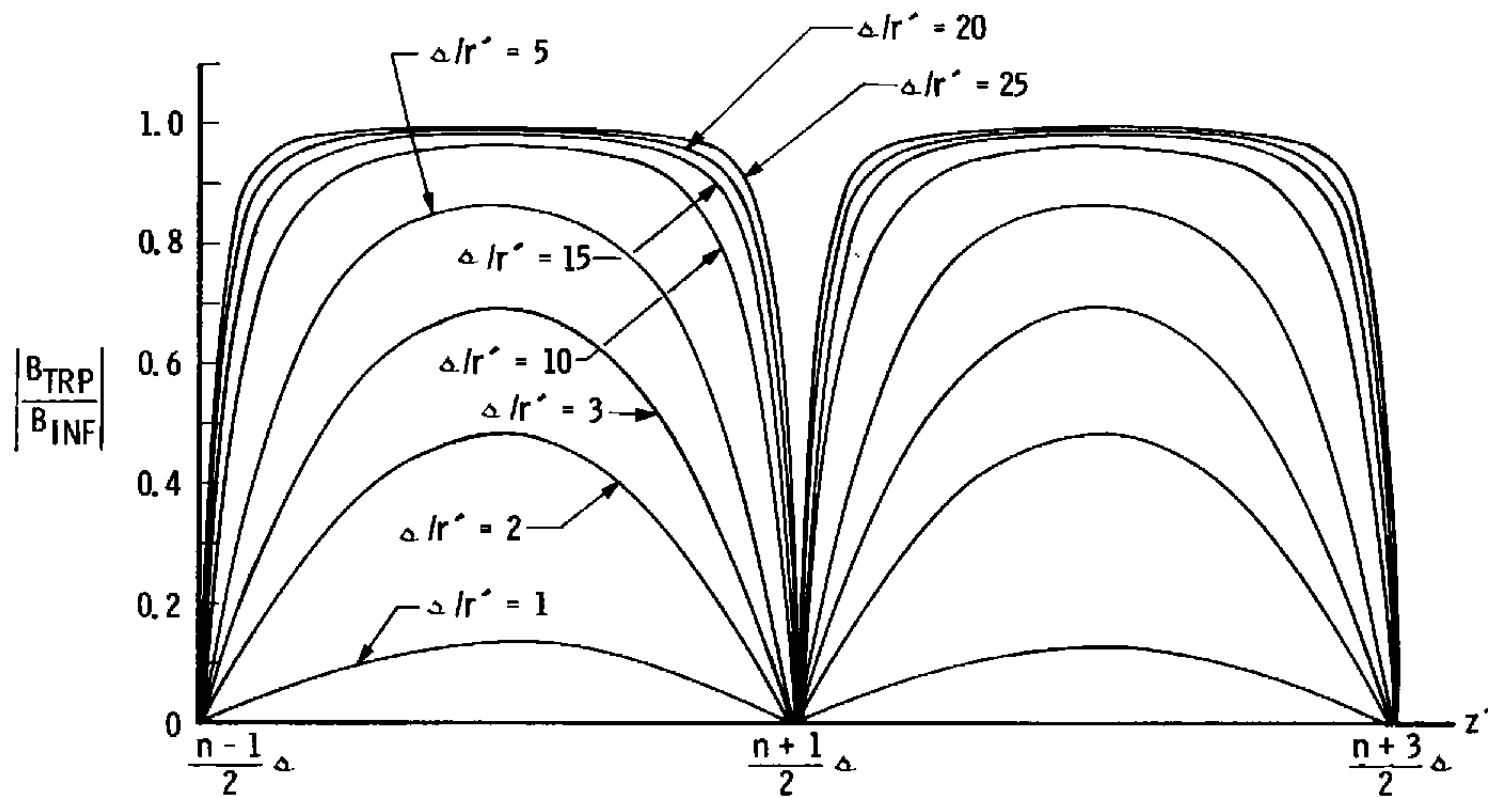
Figure 9. Magnetic field of line currents versus field of current segments.
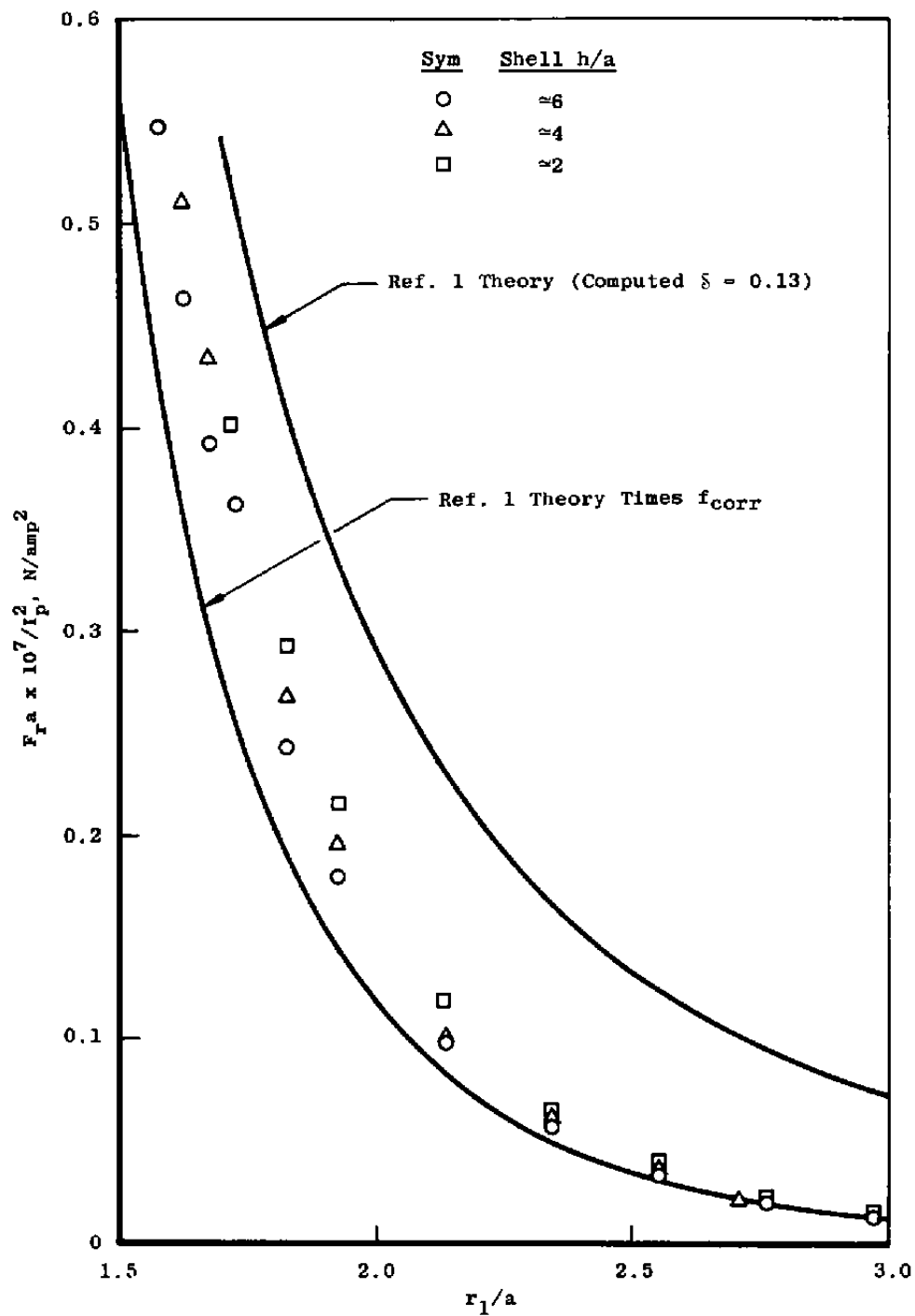
a. 1,750 rpm
Figure 10. Repulsive forces versus theory.
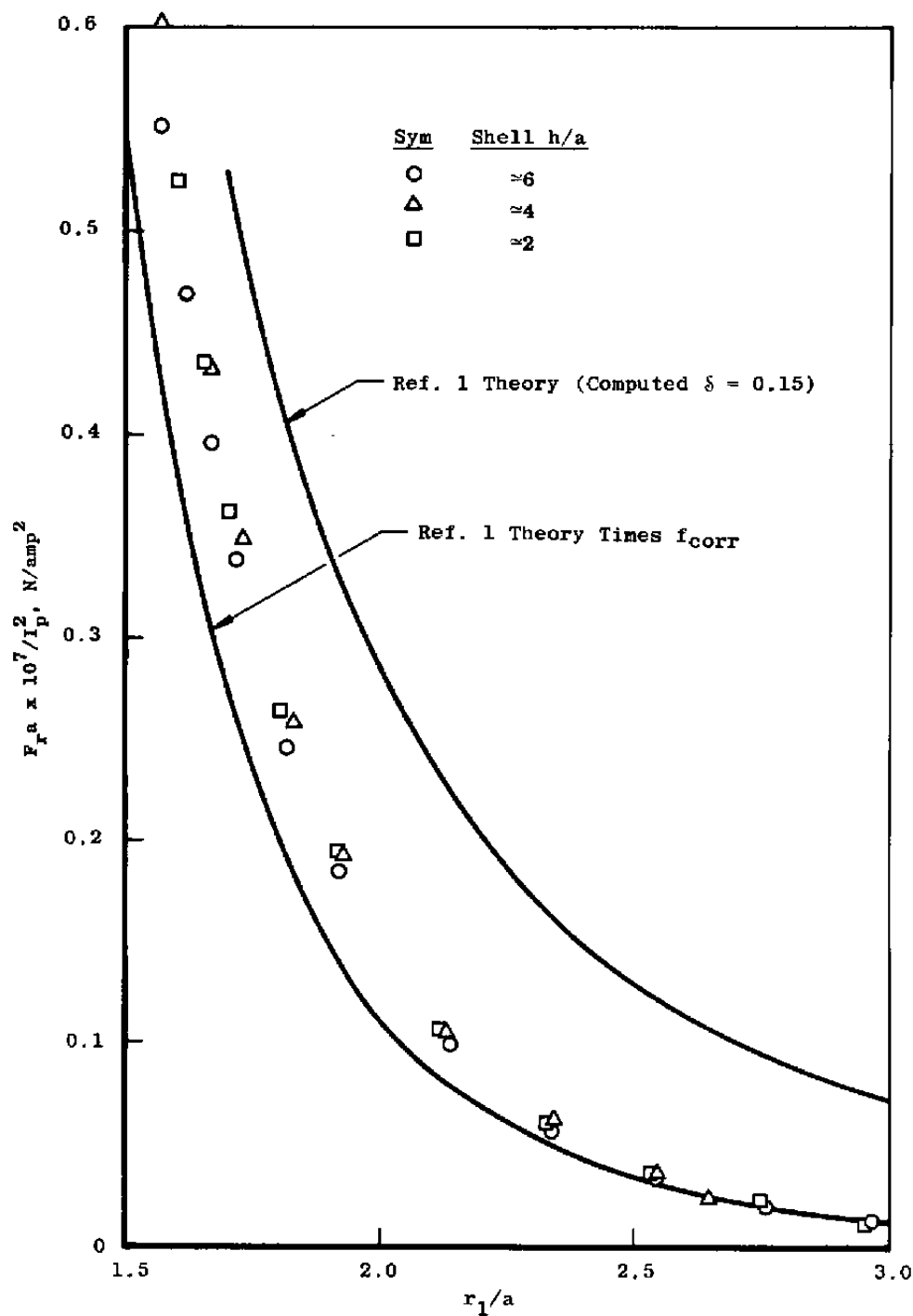
b. 1,500 rpm
Figure 10. Continued.

31
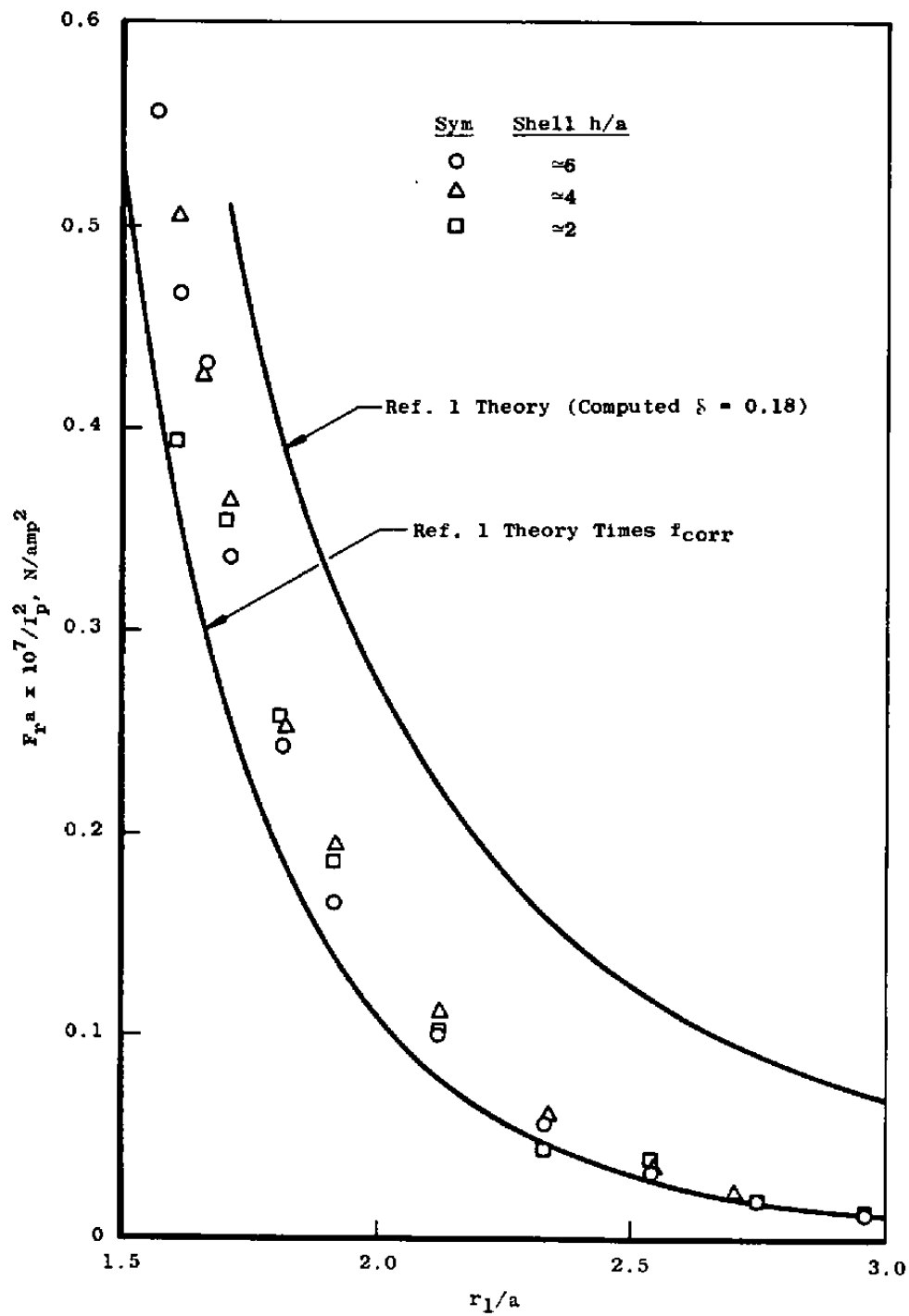
c. 1,250 rpm
Figure 10. Continued.
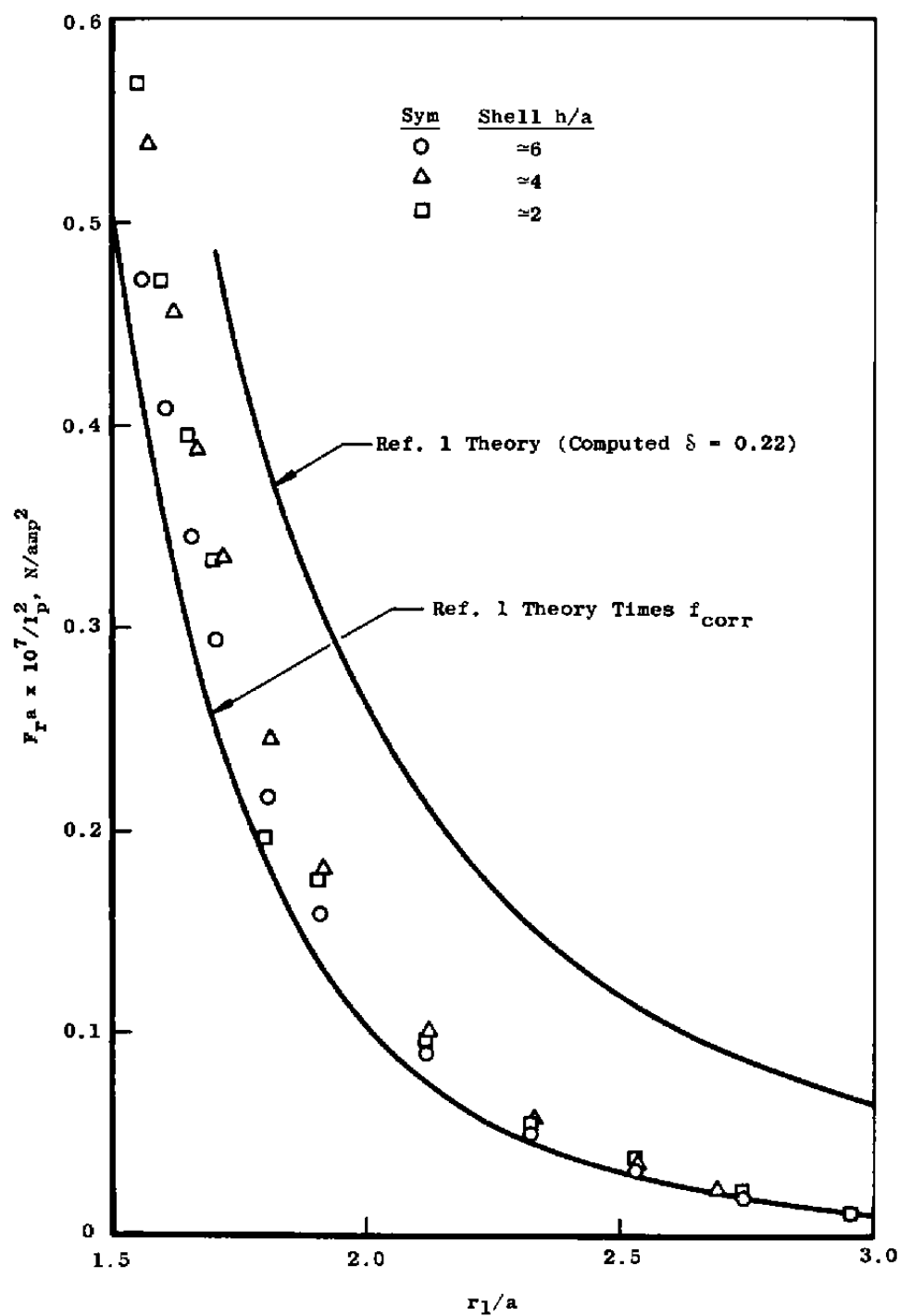
d. 1,000 rpm
Figure 10. Continued.

33
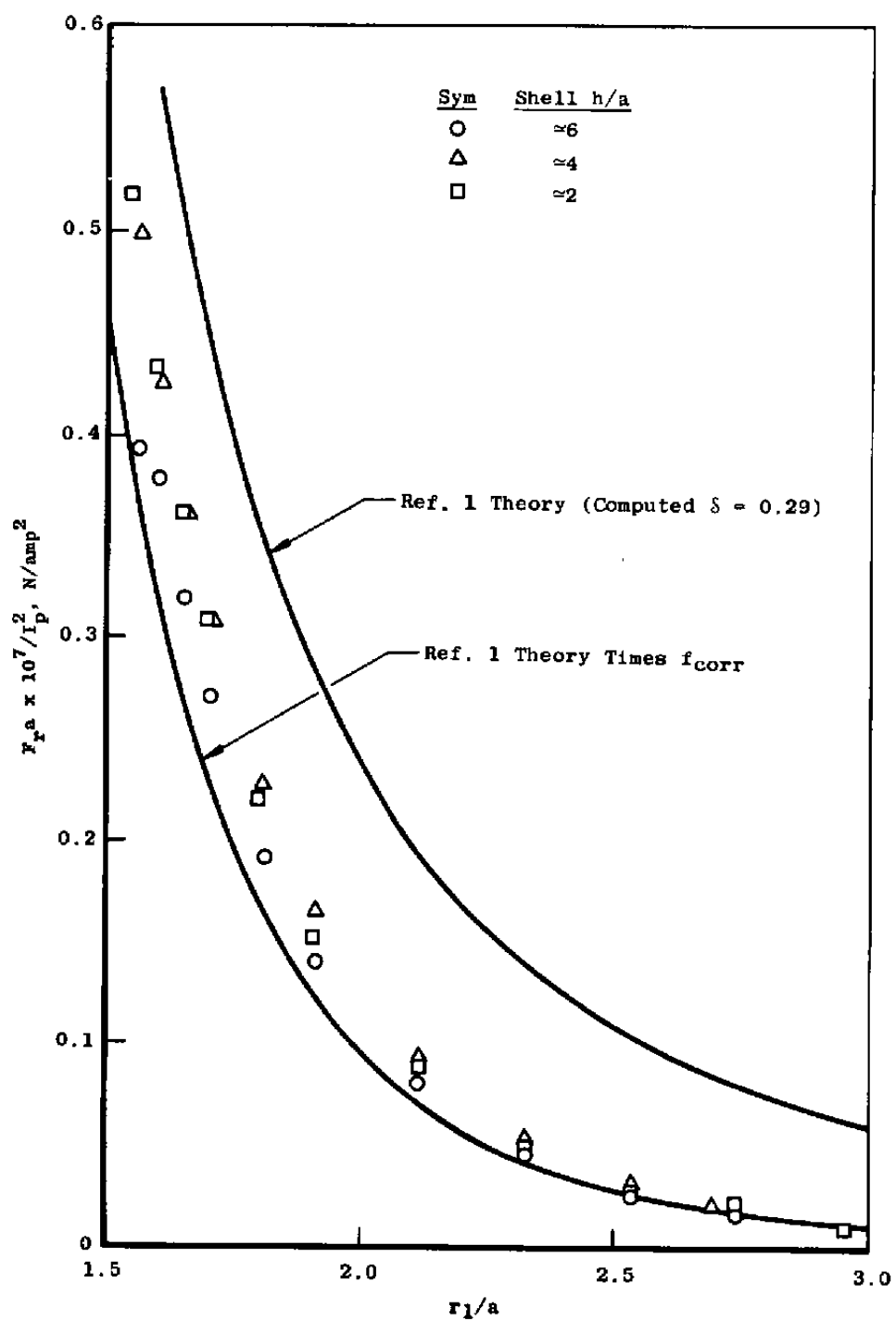
e. 750 rpm
Figure 10. Continued.

34
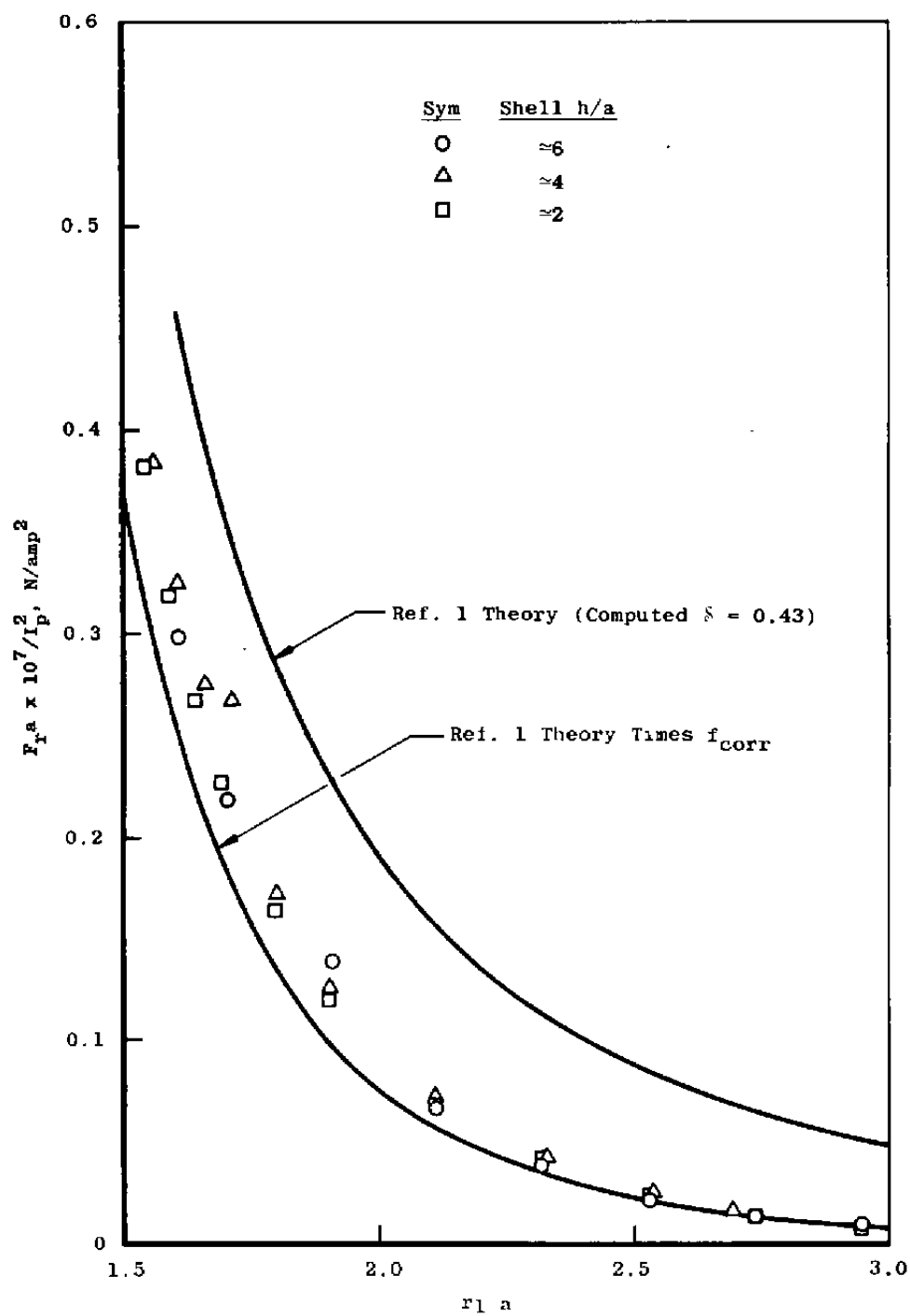
f. 500 rpm

Figure 10. Continued.
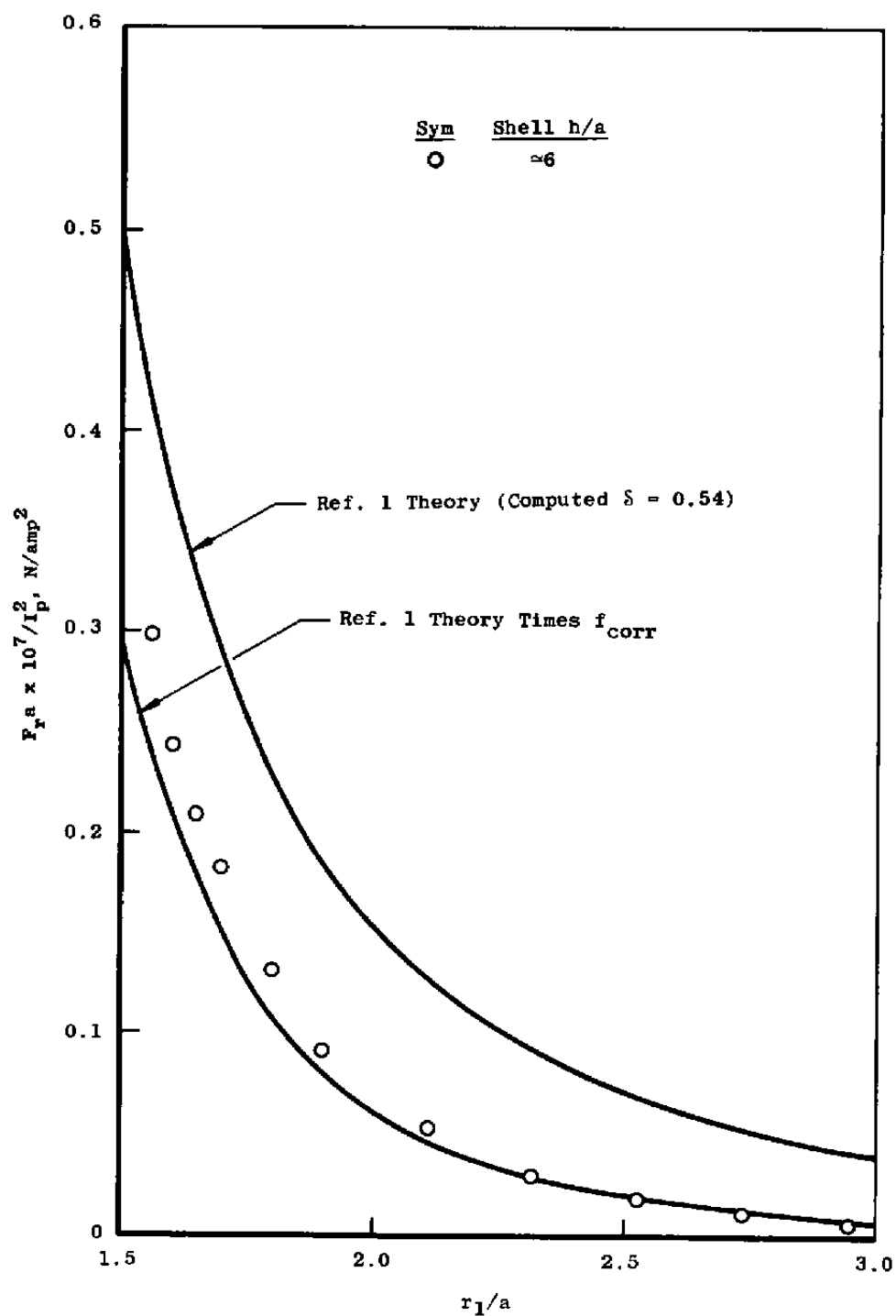
g. 350 rpm
Figure 10. Continued.
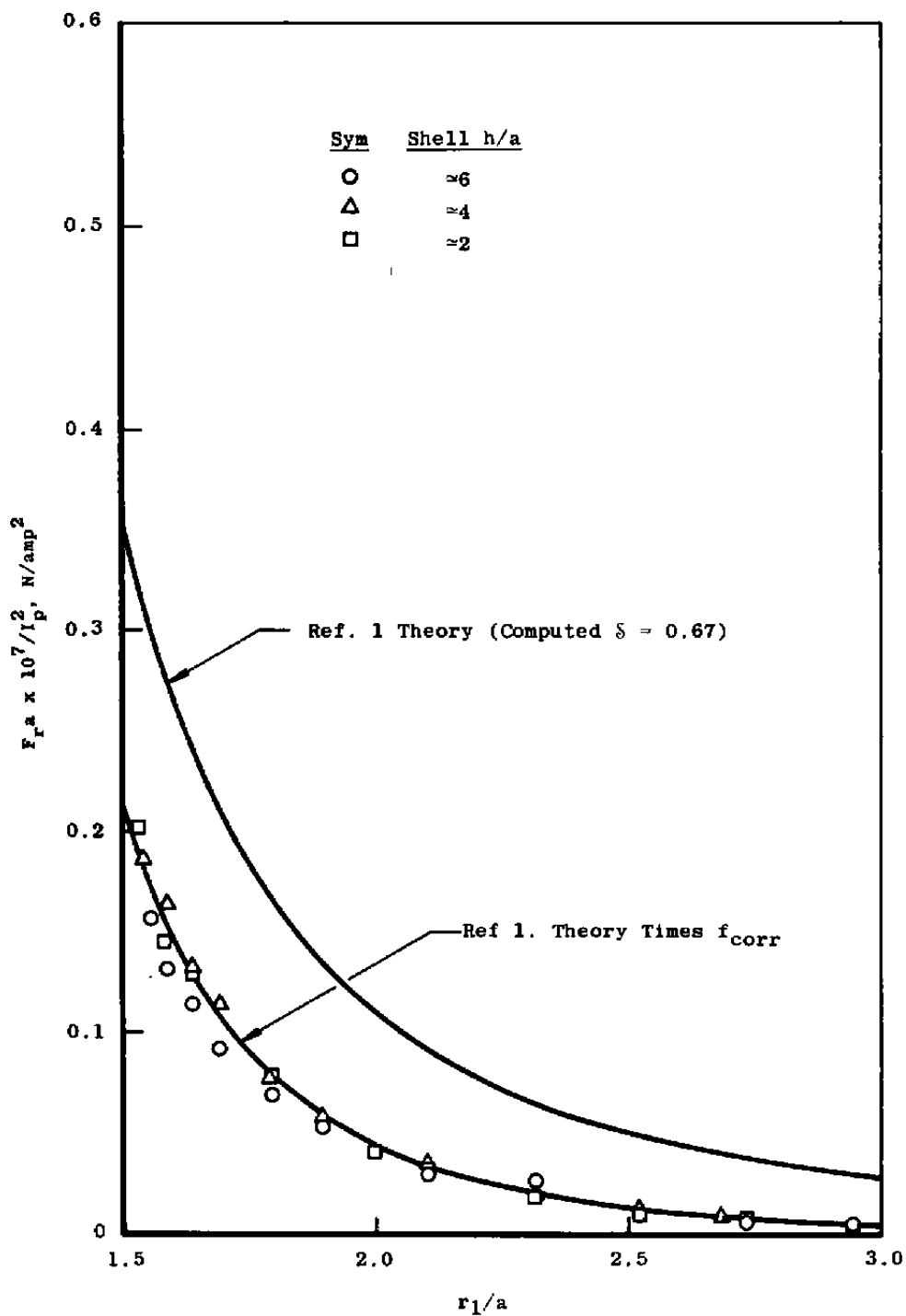
h. 250 rpm
Figure 10. Concluded.
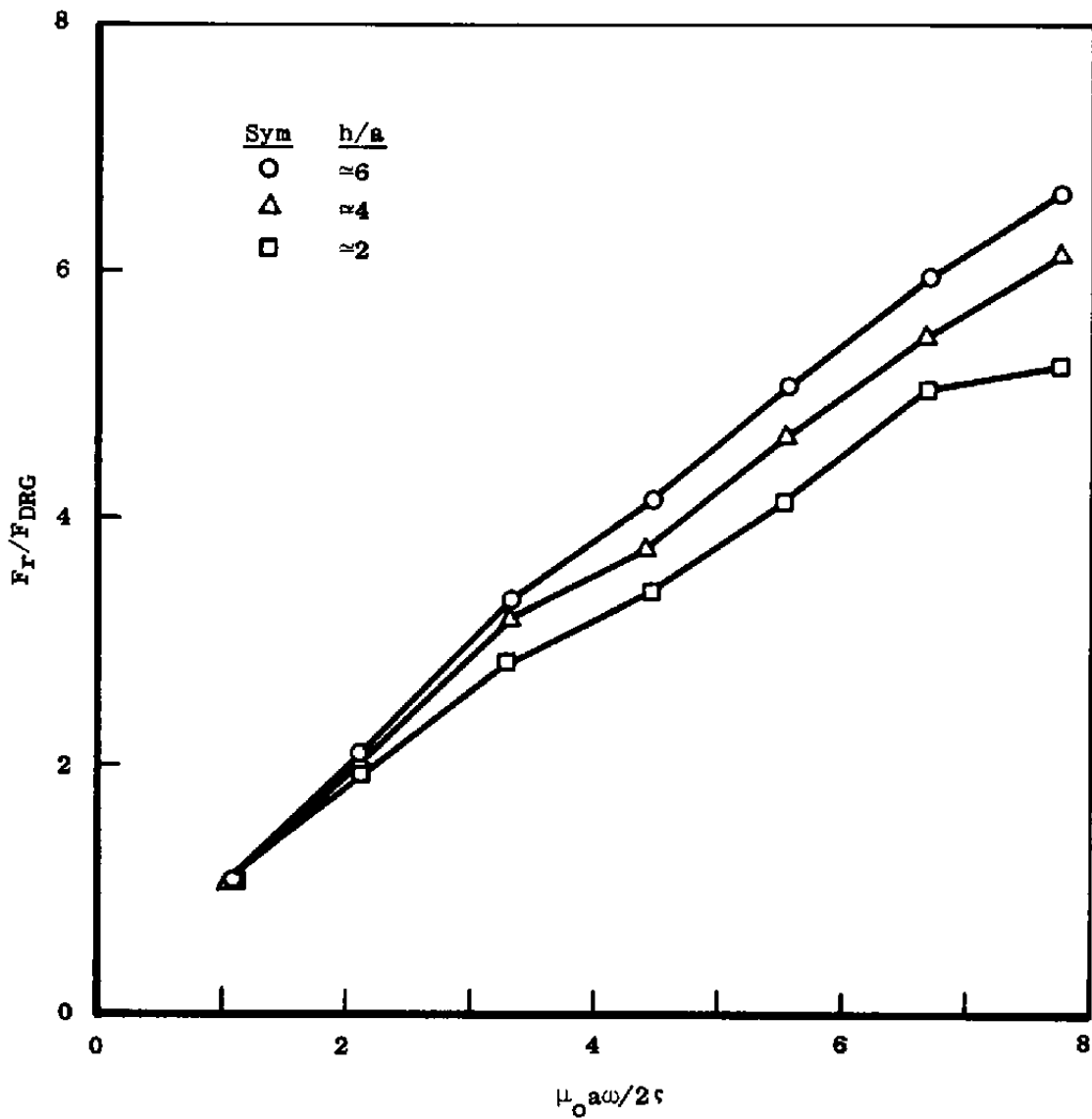
a. $r_1/a \simeq 1.55$
Figure 11. Ratio of repulsive to drag forces.
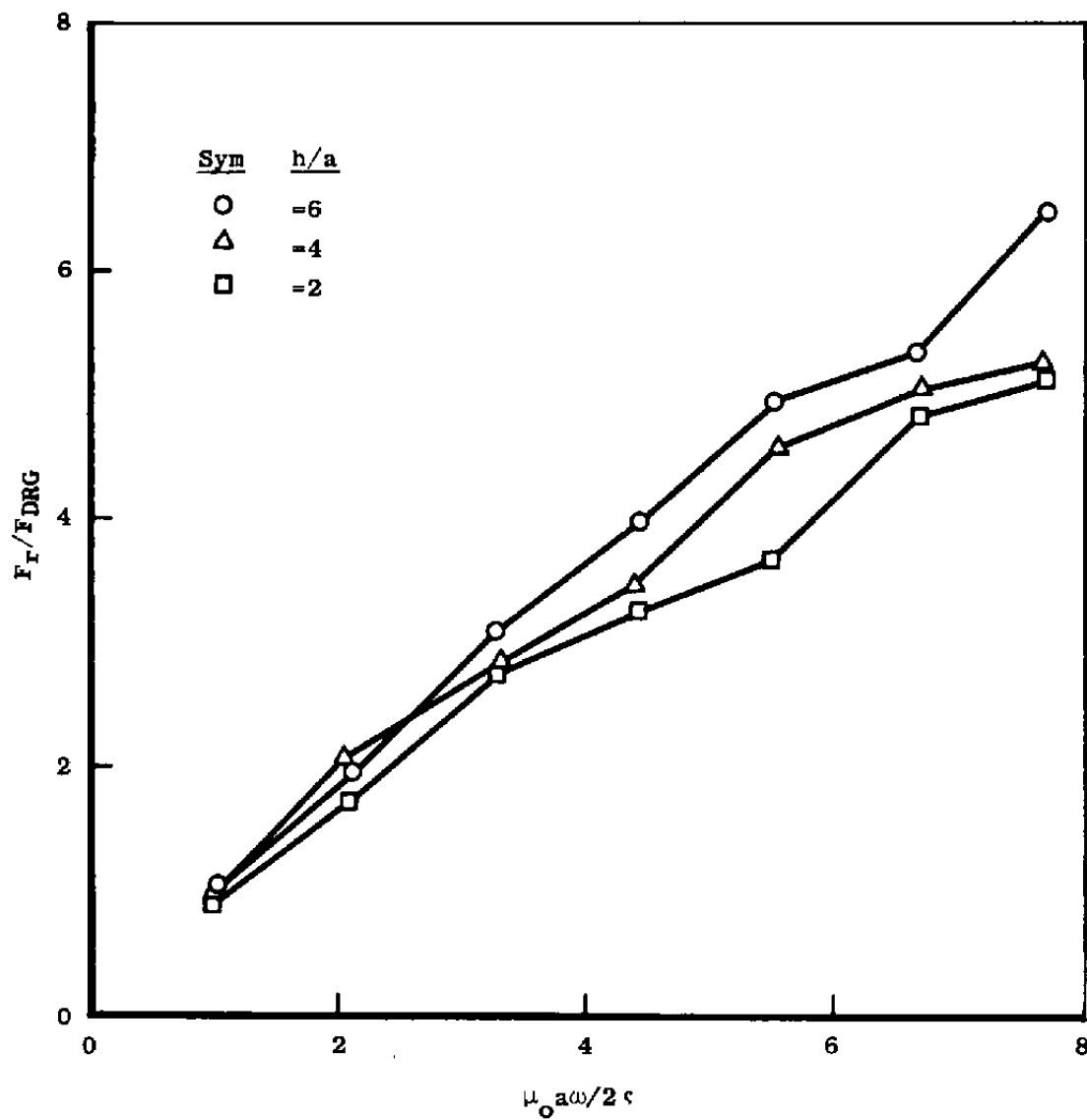
b. $r_1/a = 1.92$
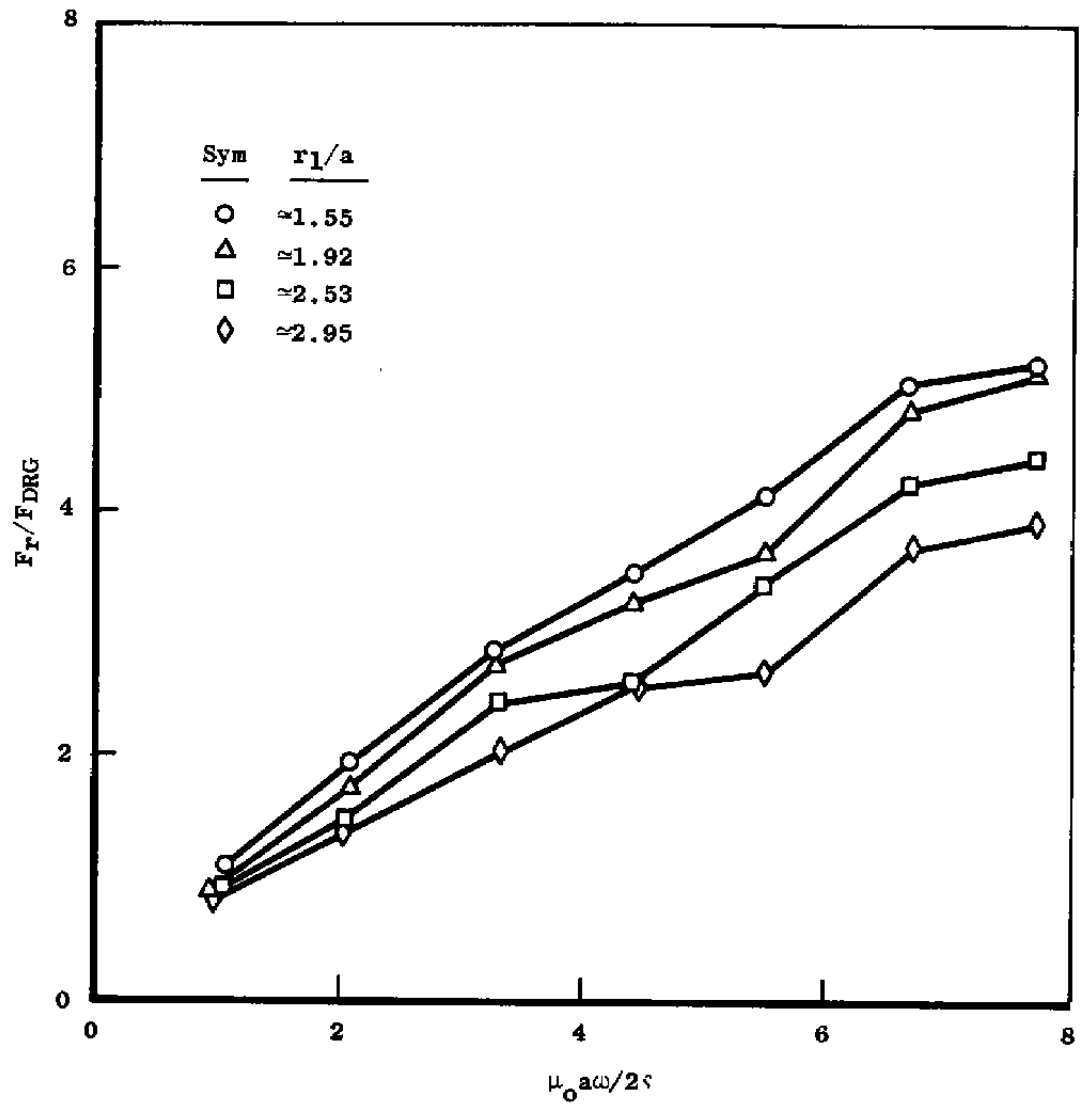Figure 11. Continued.
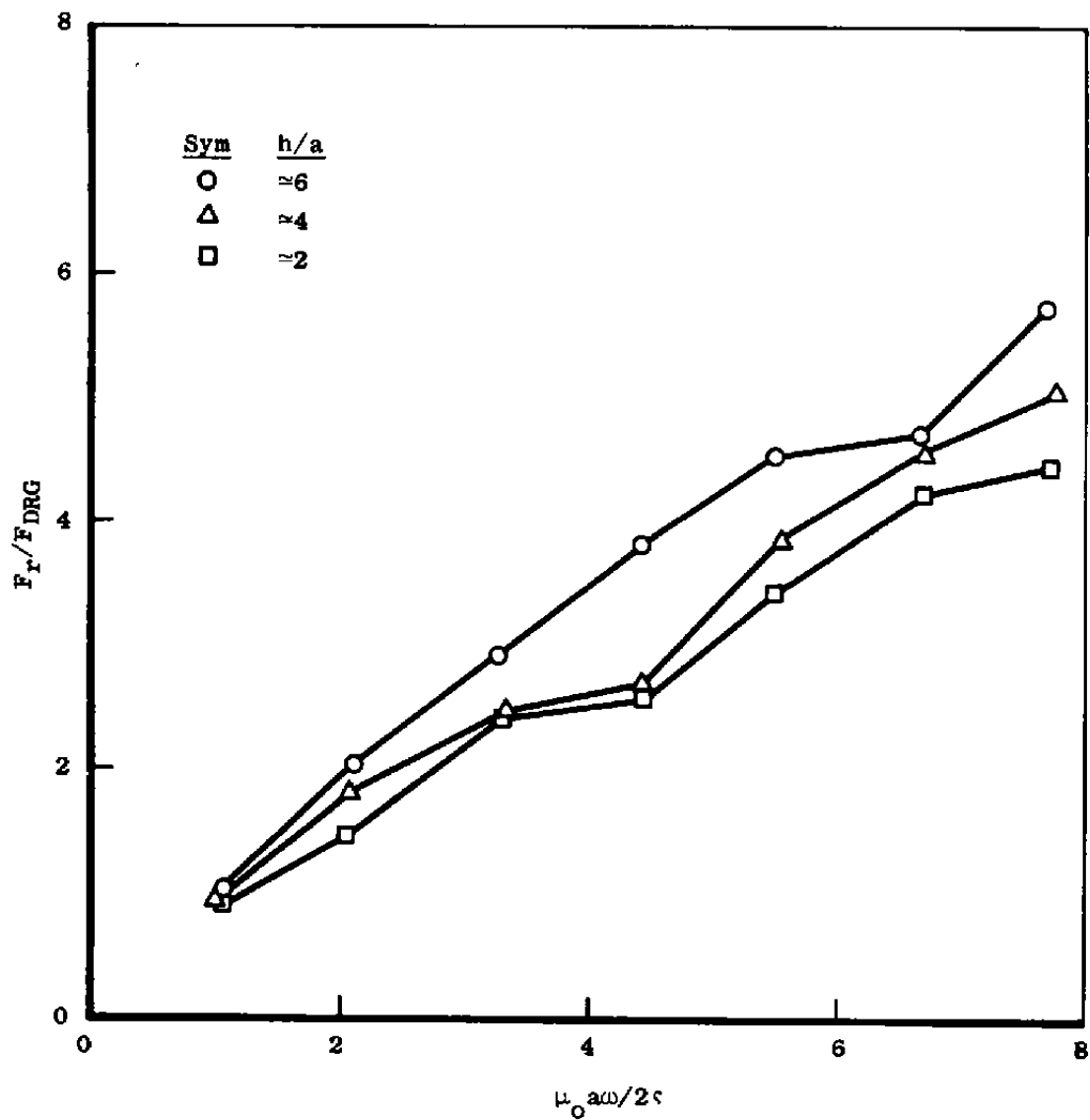
c. $r_1/a = 2.53$
Figure 11. Concluded.
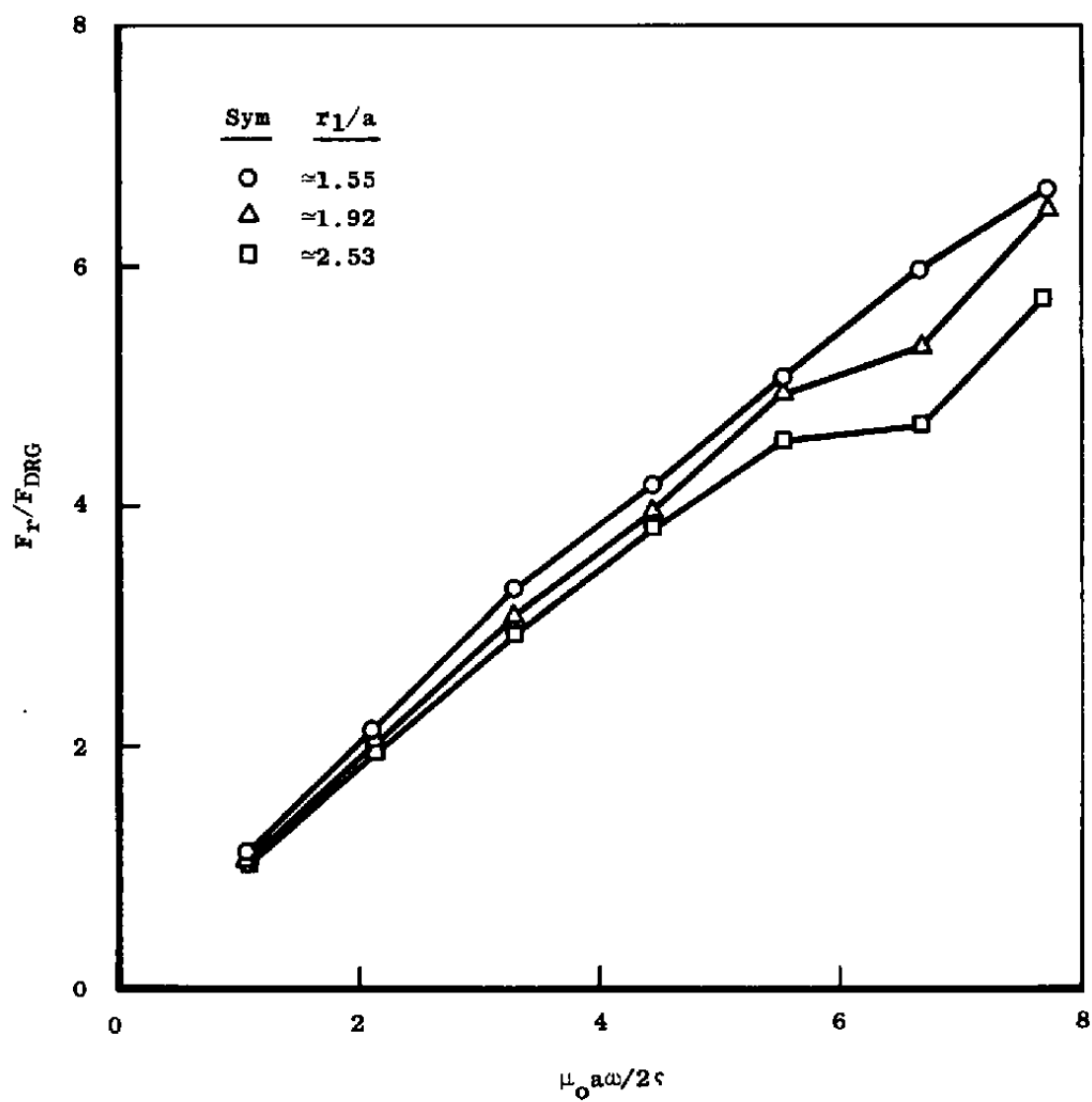
a. h/a ≃ 6
Figure 12. Ratio of repulsive to drag forces.
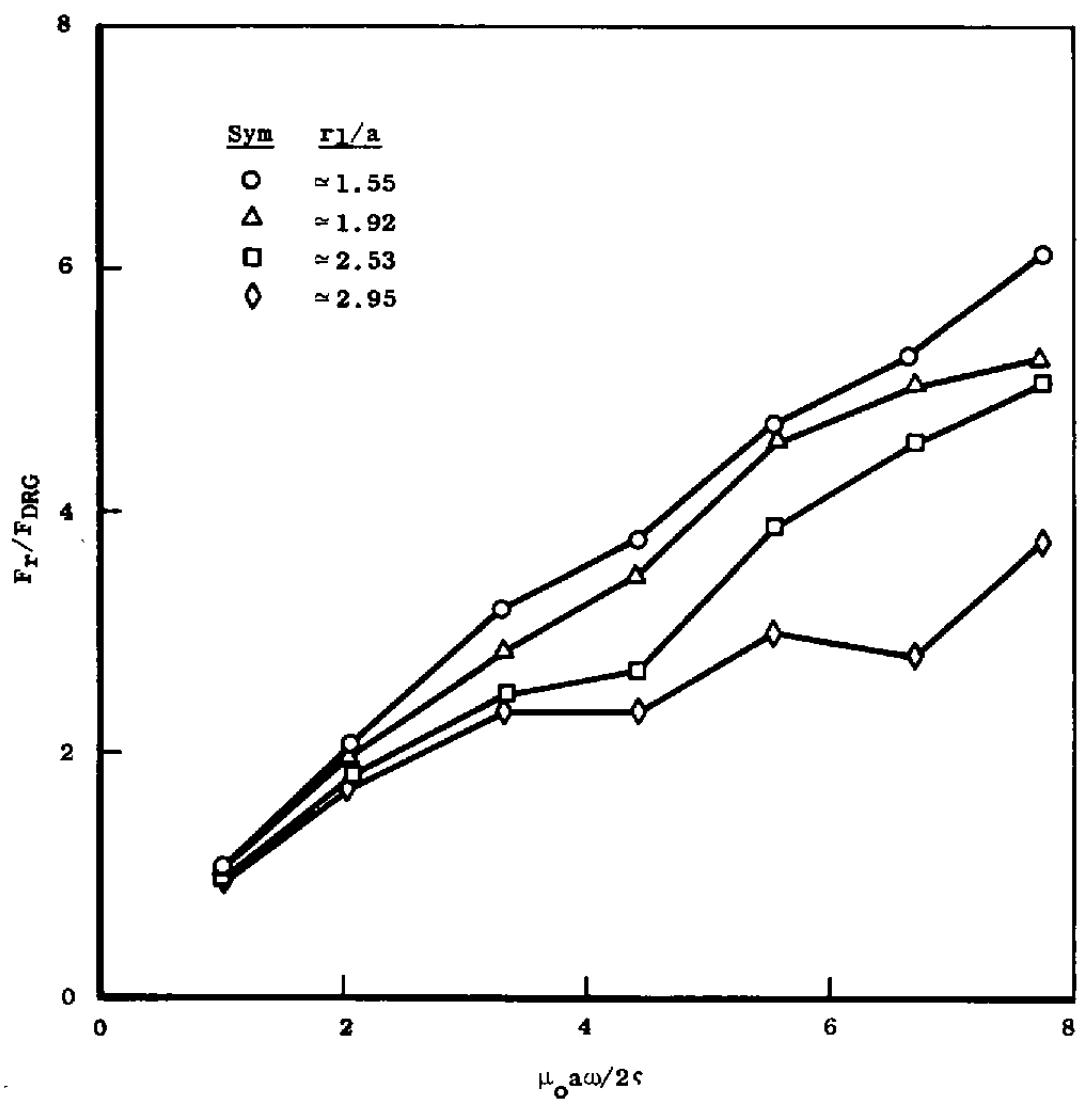
b. $h/a \simeq 4$
Figure 12. Continued.

c. h/a $\simeq$ 2
Figure 12. Concluded.
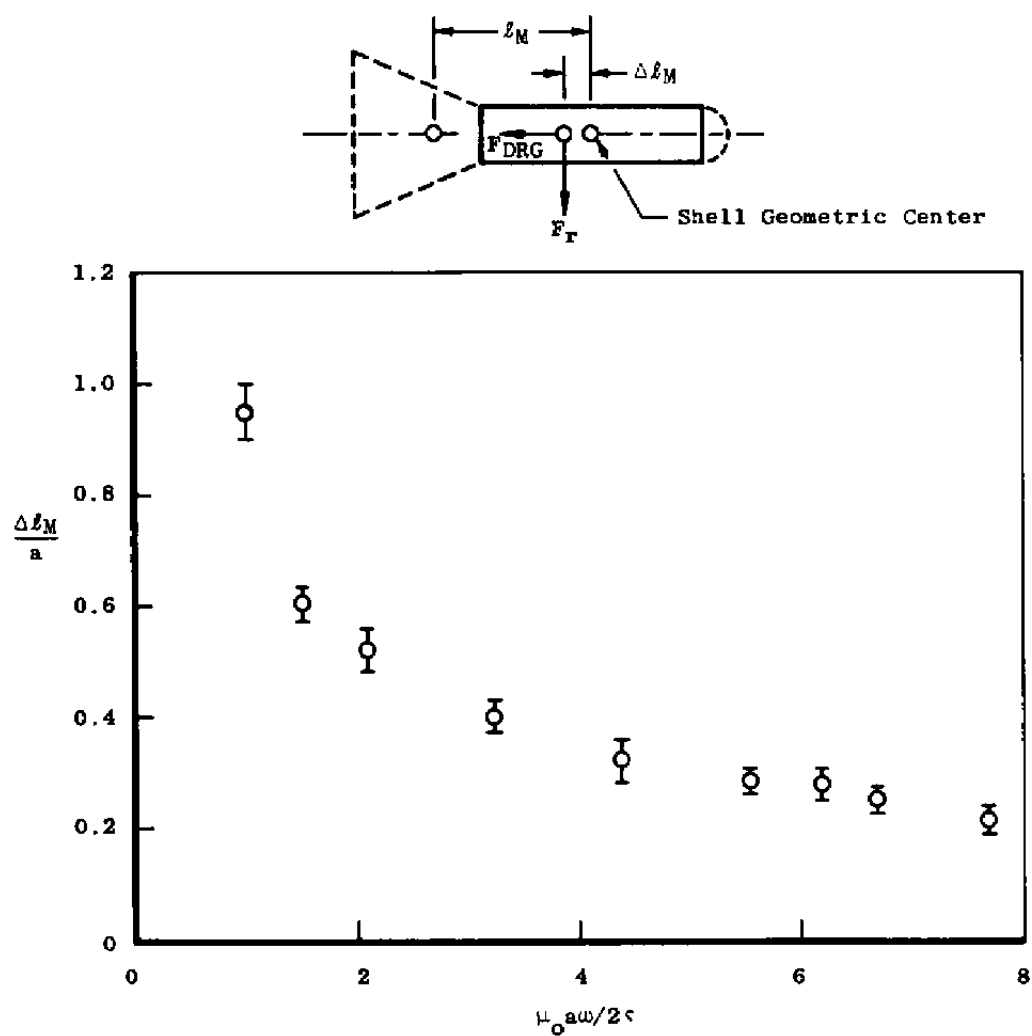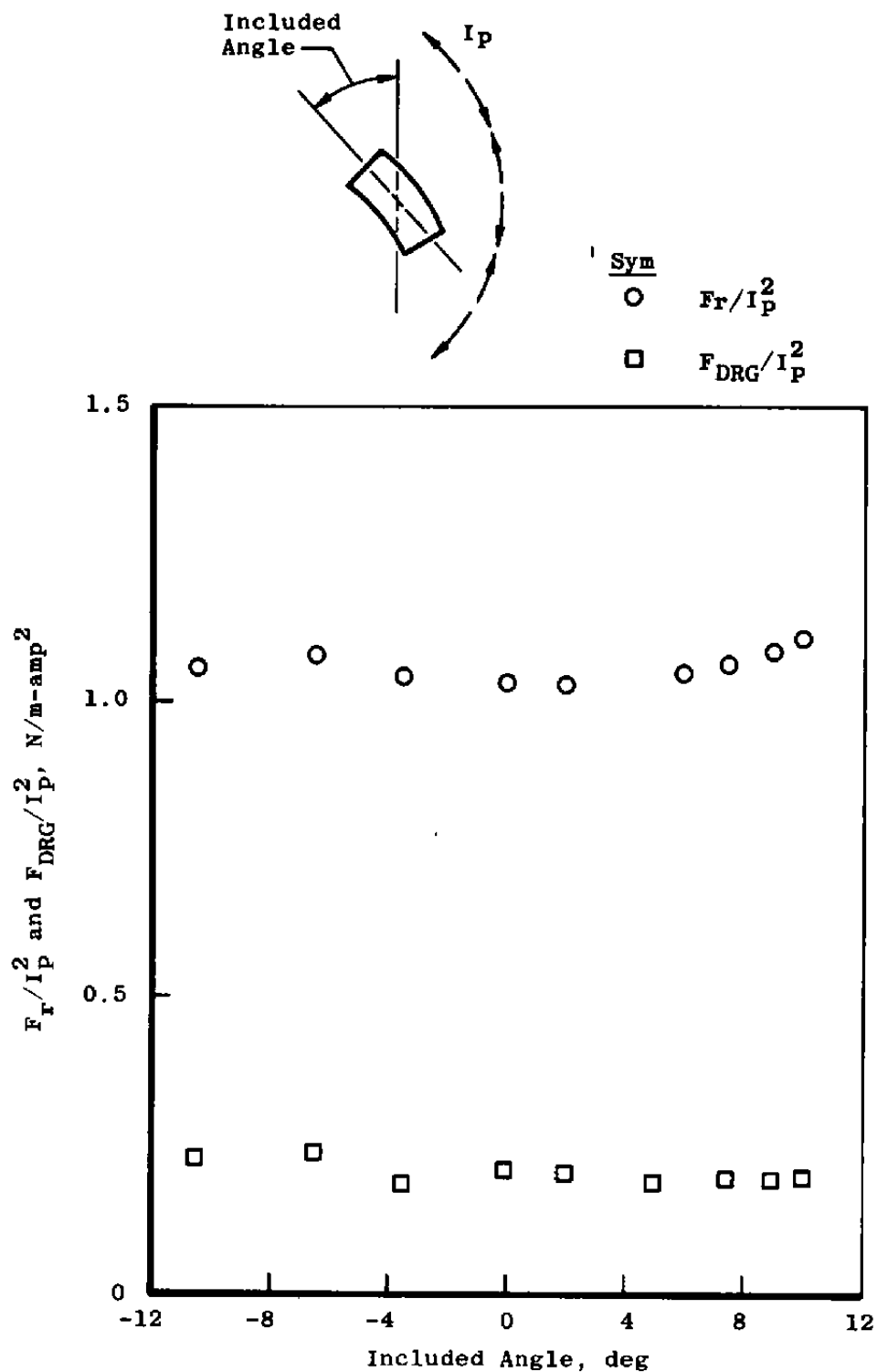
Figure 13. Magnetic moment arm versus correlation parameter.

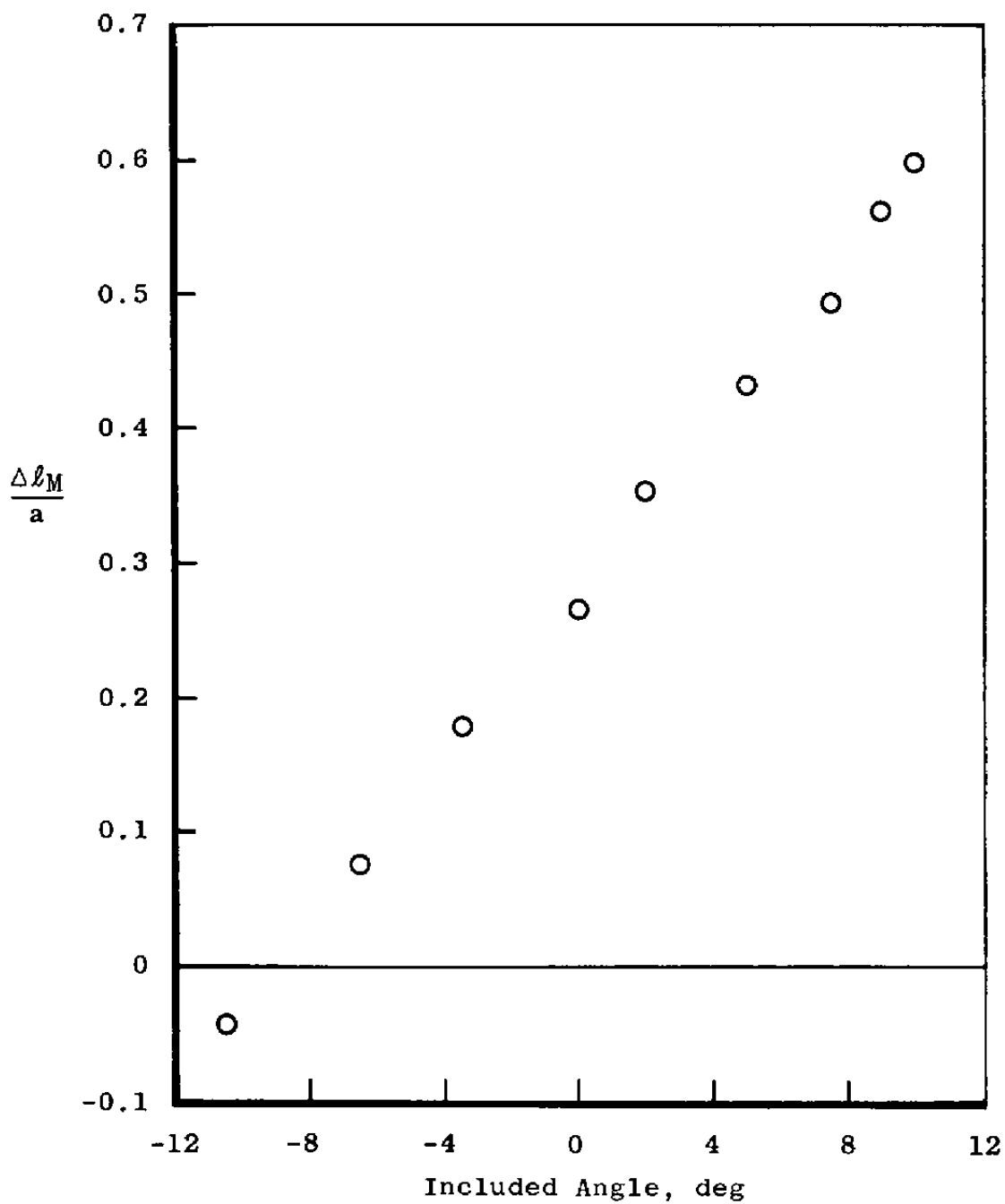Figure 14. Effect of misalignment on positional and drag forces.

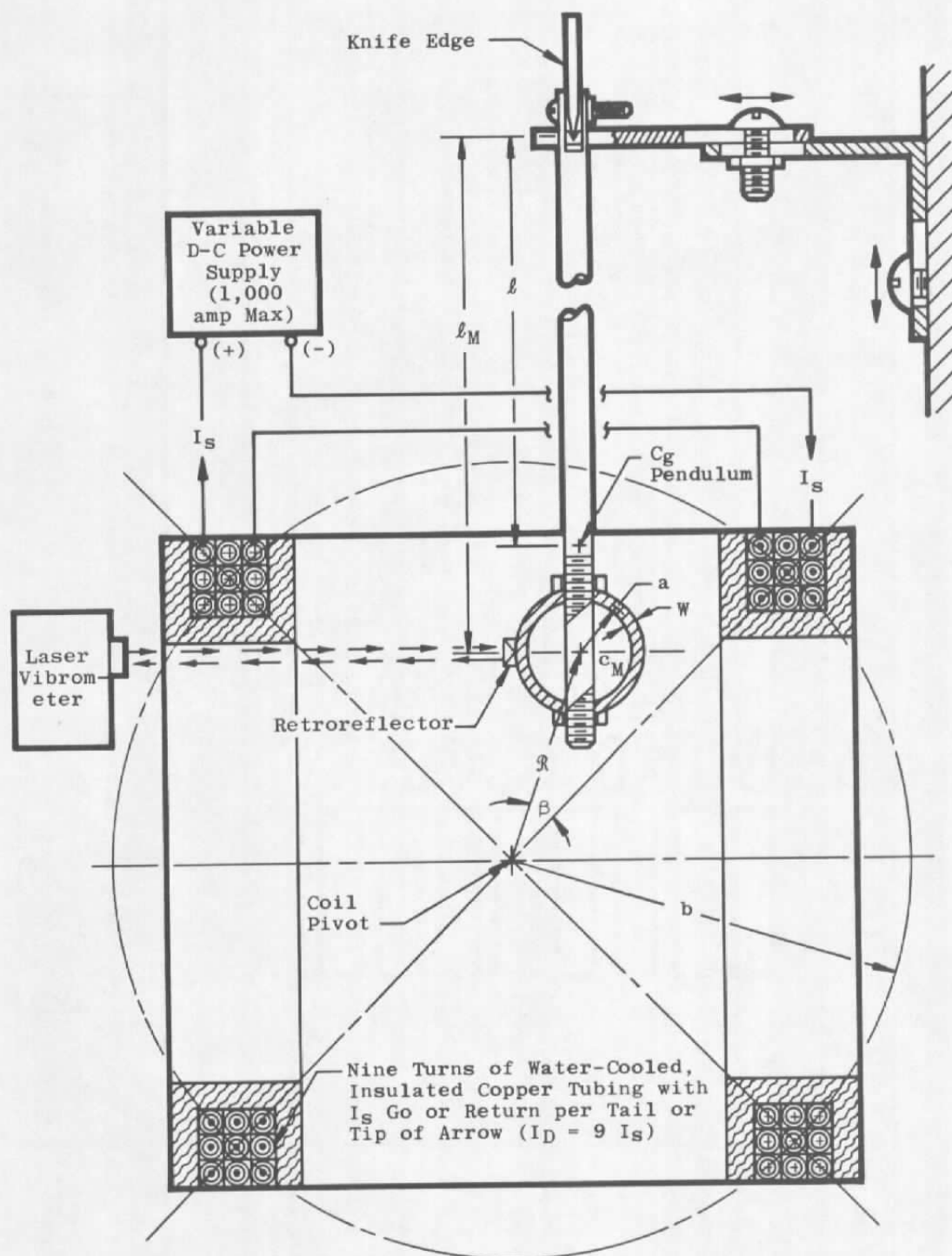Figure 15. Effect of misalignment on magnetic moment arm.
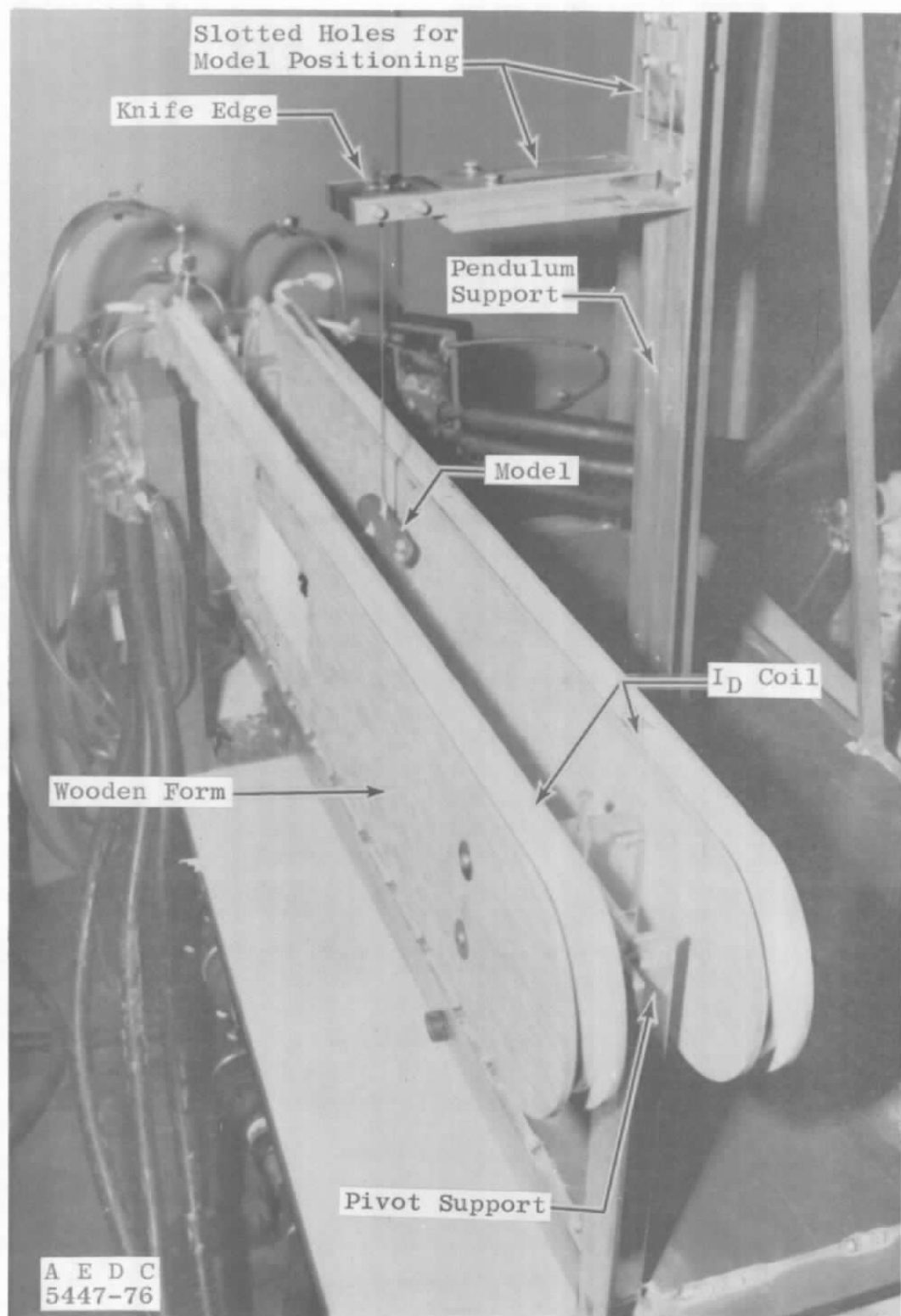
Figure 16. Sketch of damping force apparatus.

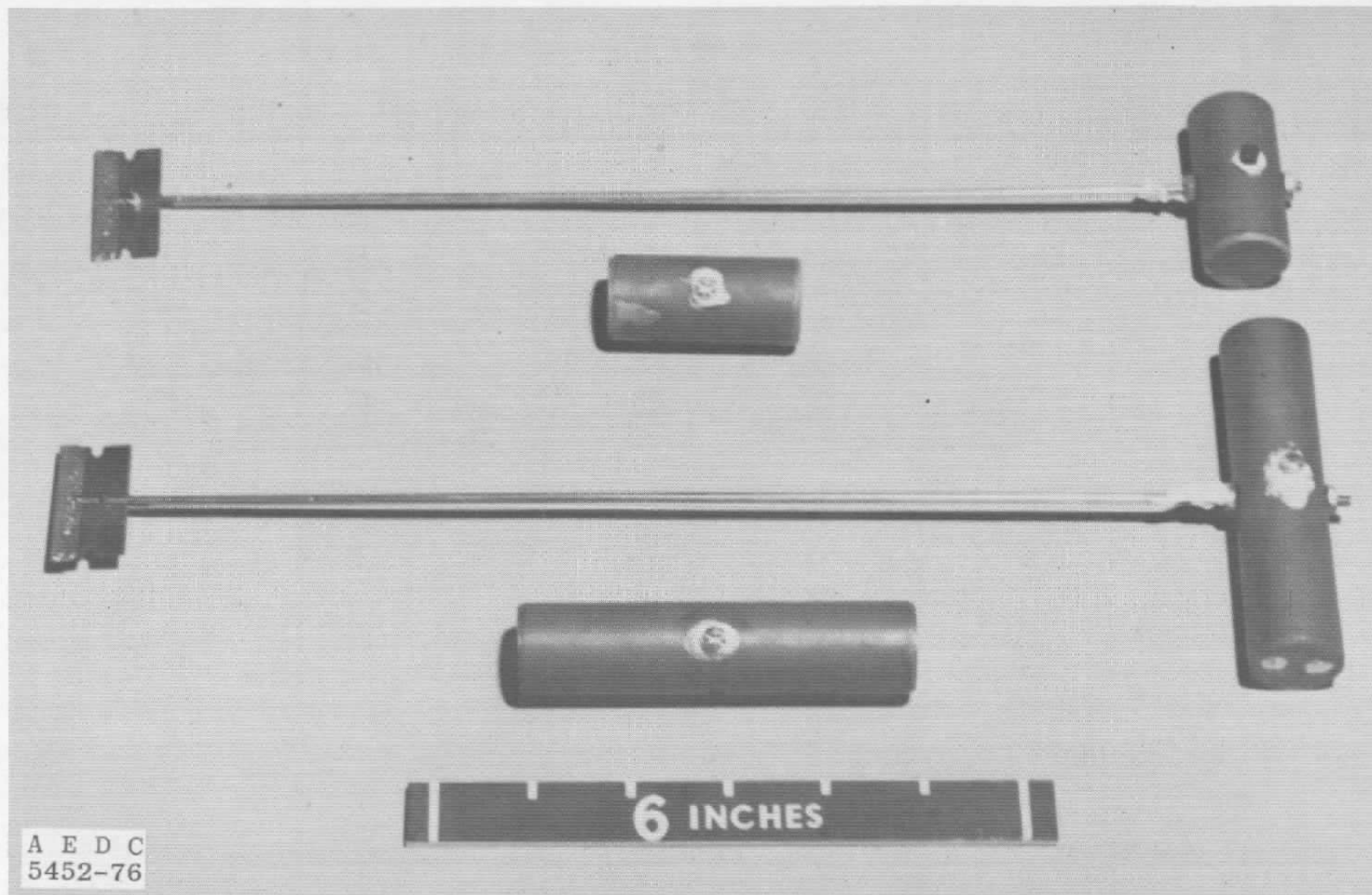Figure 17. Photograph of damping force apparatus.

6 INCHES

Figure 18. Photograph of conductive shells for damping forces.
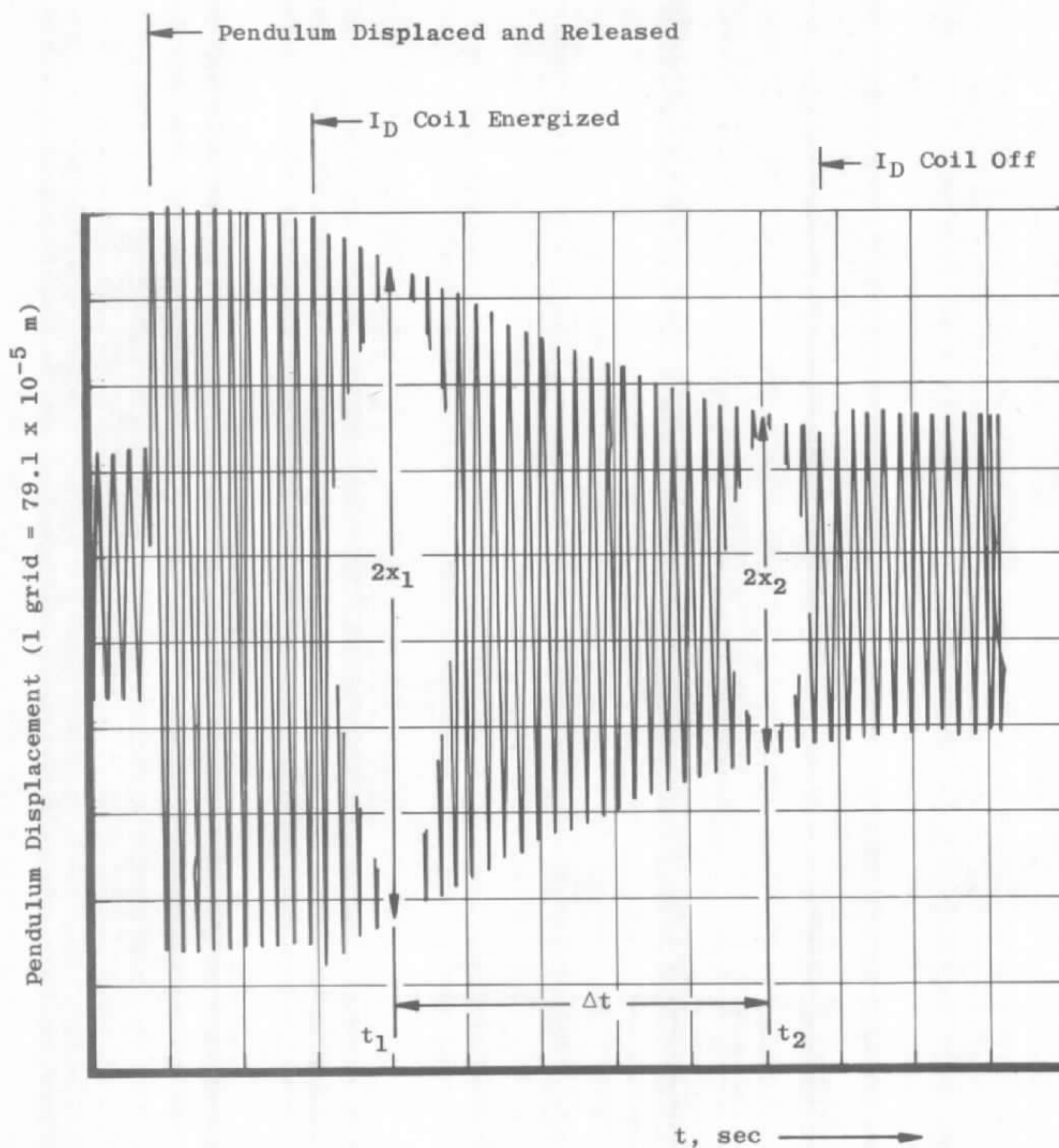
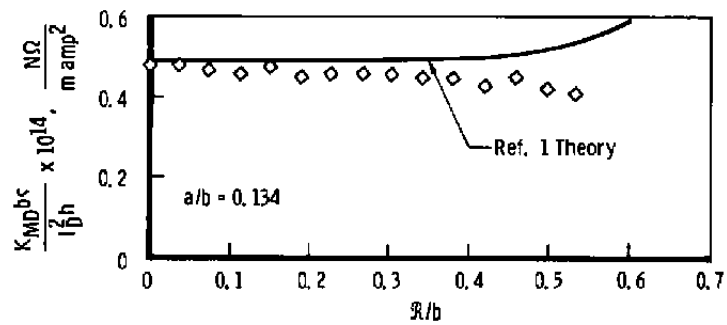Figure 19. Representative damping pattern of pendulum (strip chart).

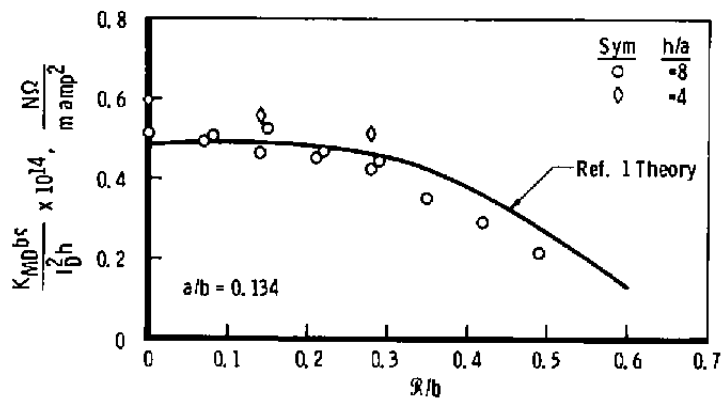a. Thick shell, $\beta = \pi/8$

b. Thick shell, $\beta = \pi/4$

c. Thin shell, $\beta = \pi/4$
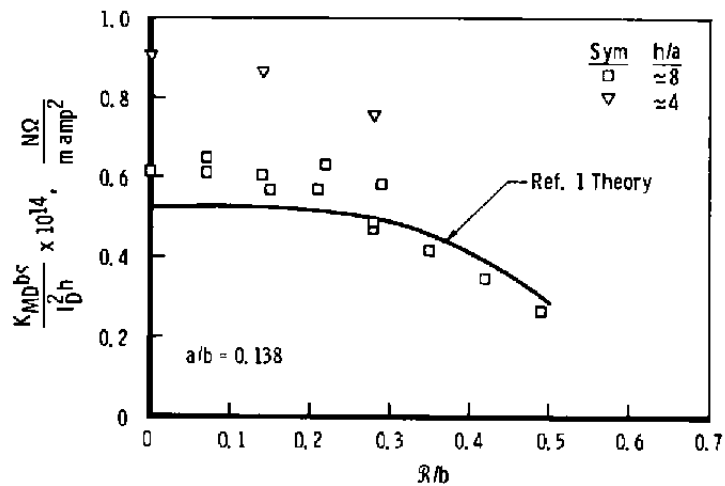Figure 20. Radial damping coefficients.

51
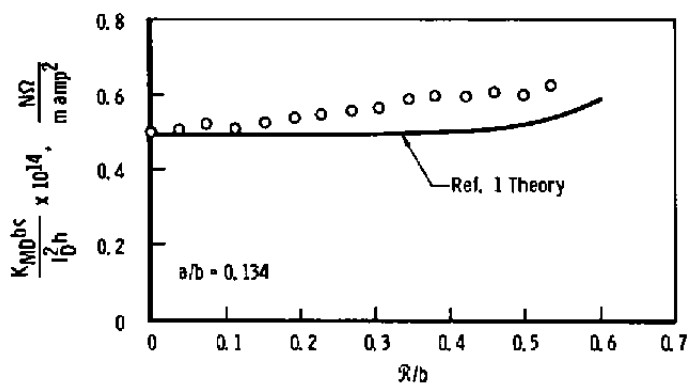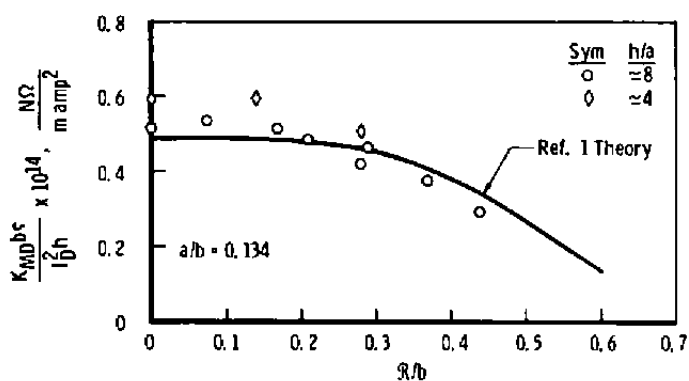
a. Thick shell, $\beta = \pi/8$
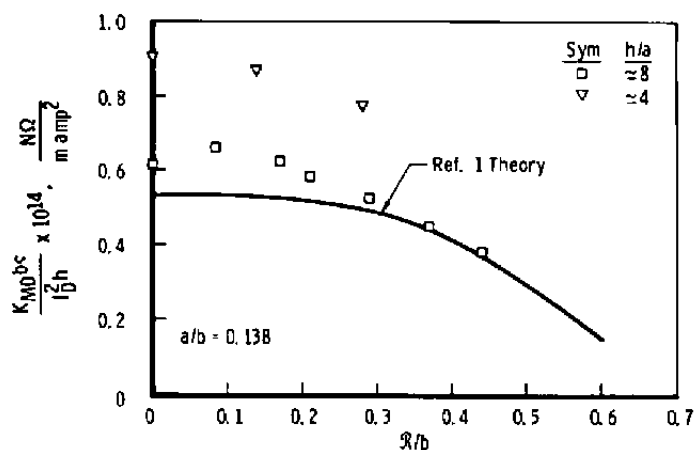
b. Thick shell, $\beta = \pi/4$

c. Thin shell, $\beta = \pi/4$
Figure 21. Angular damping coefficient.
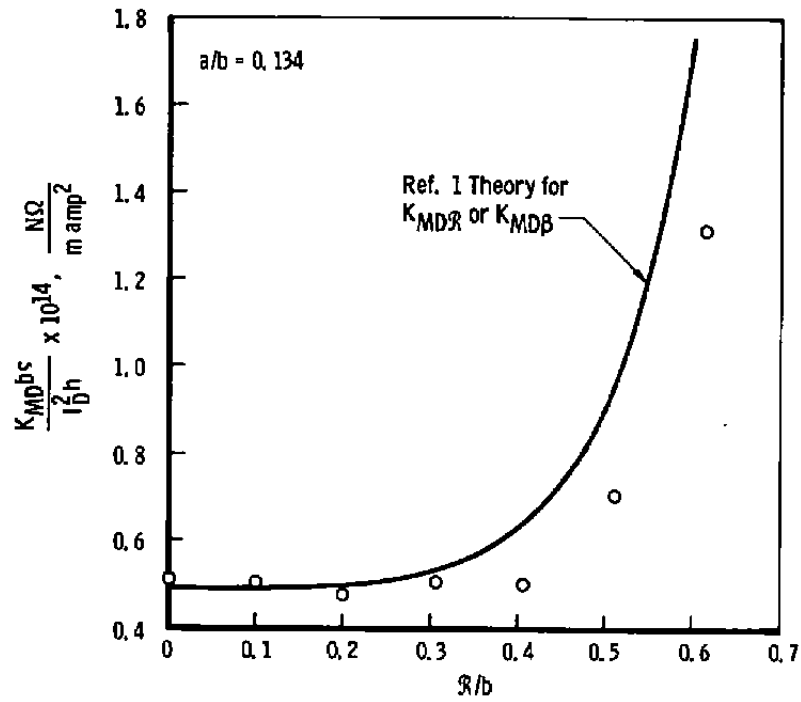
a. Thick shell, $\beta = 0$
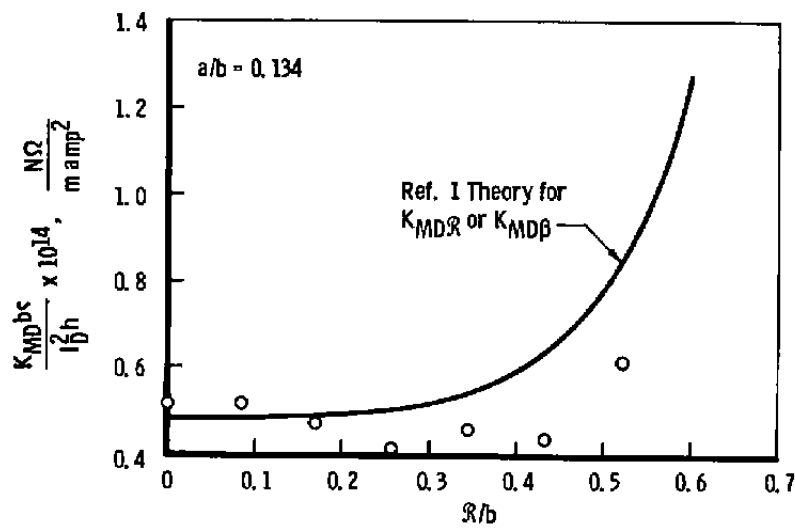
b. Thick shell, $\beta = \pi/16$

Figure 22. Combination damping coefficient.

53

c. Thick shell, $\beta = \pi/8$

d. Thick shell, $\beta = 3\pi/16$
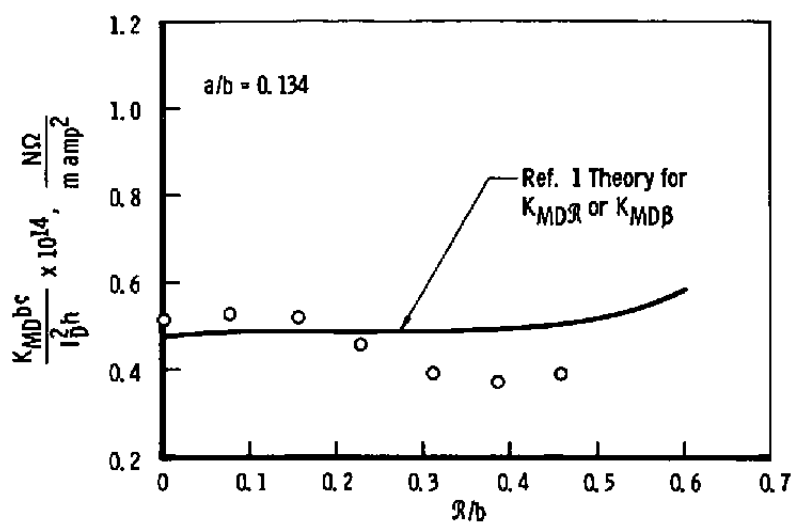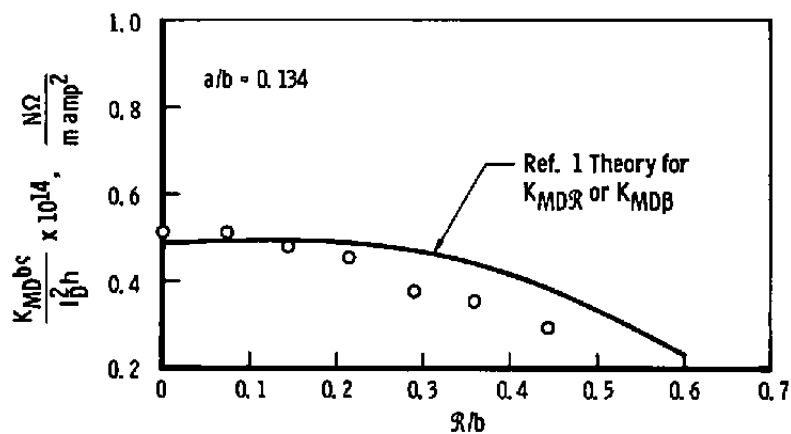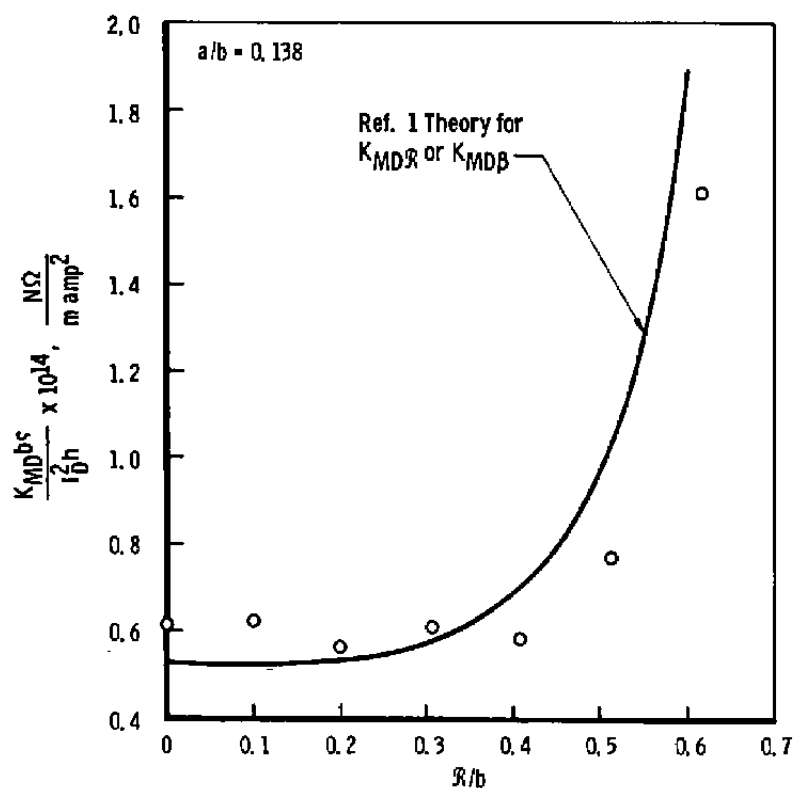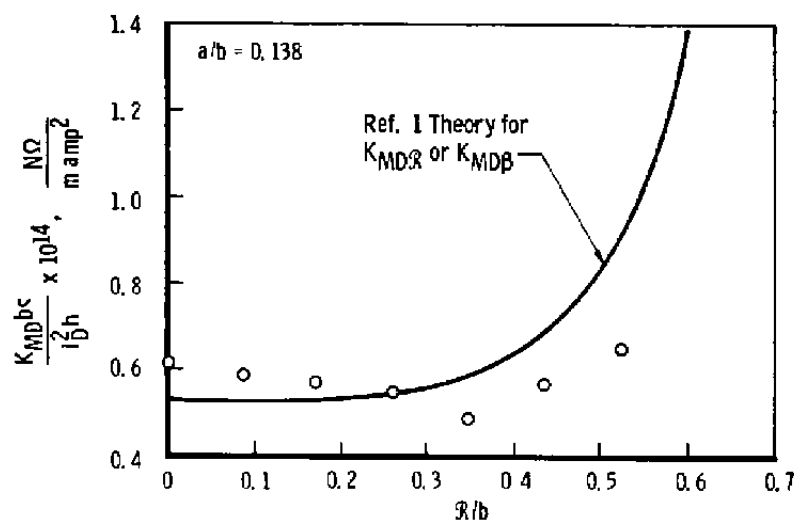Figure 22. Continued.

e. Thin shell, $\beta = 0$

f. Thin shell, $\beta = \pi/16$
Figure 22. Continued.
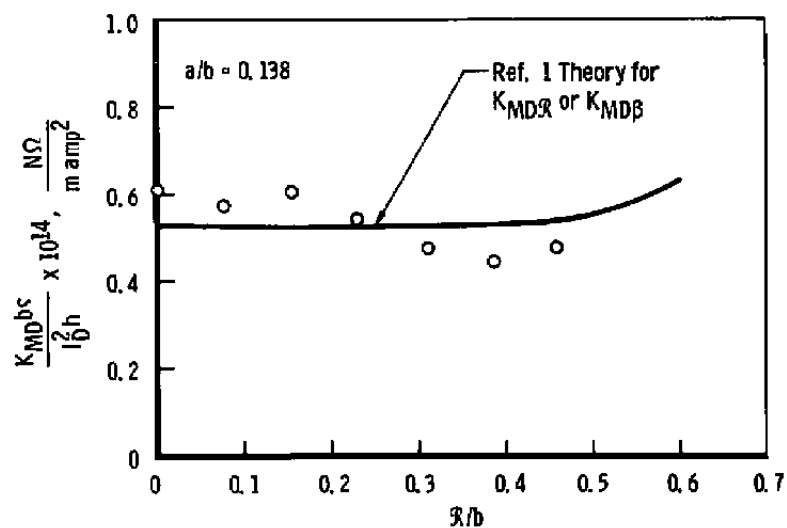
g. Thin shell, $\beta = \pi/8$
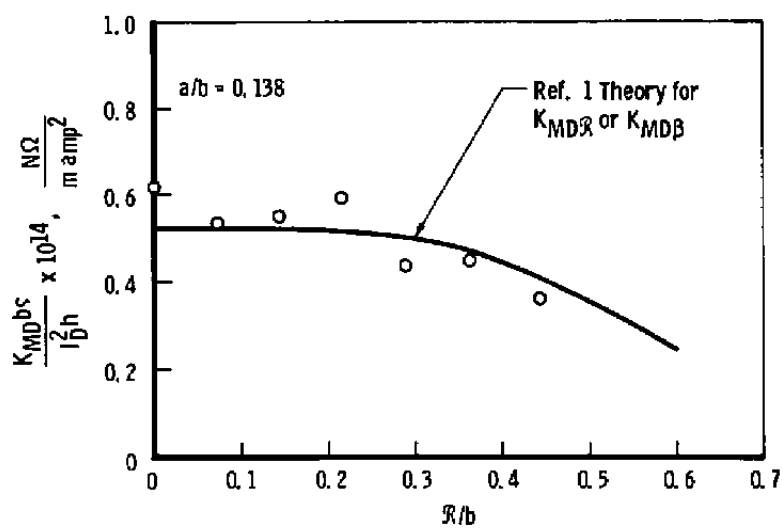
h. Thin shell, $\beta = 3\pi/16$
Figure 22. Concluded.
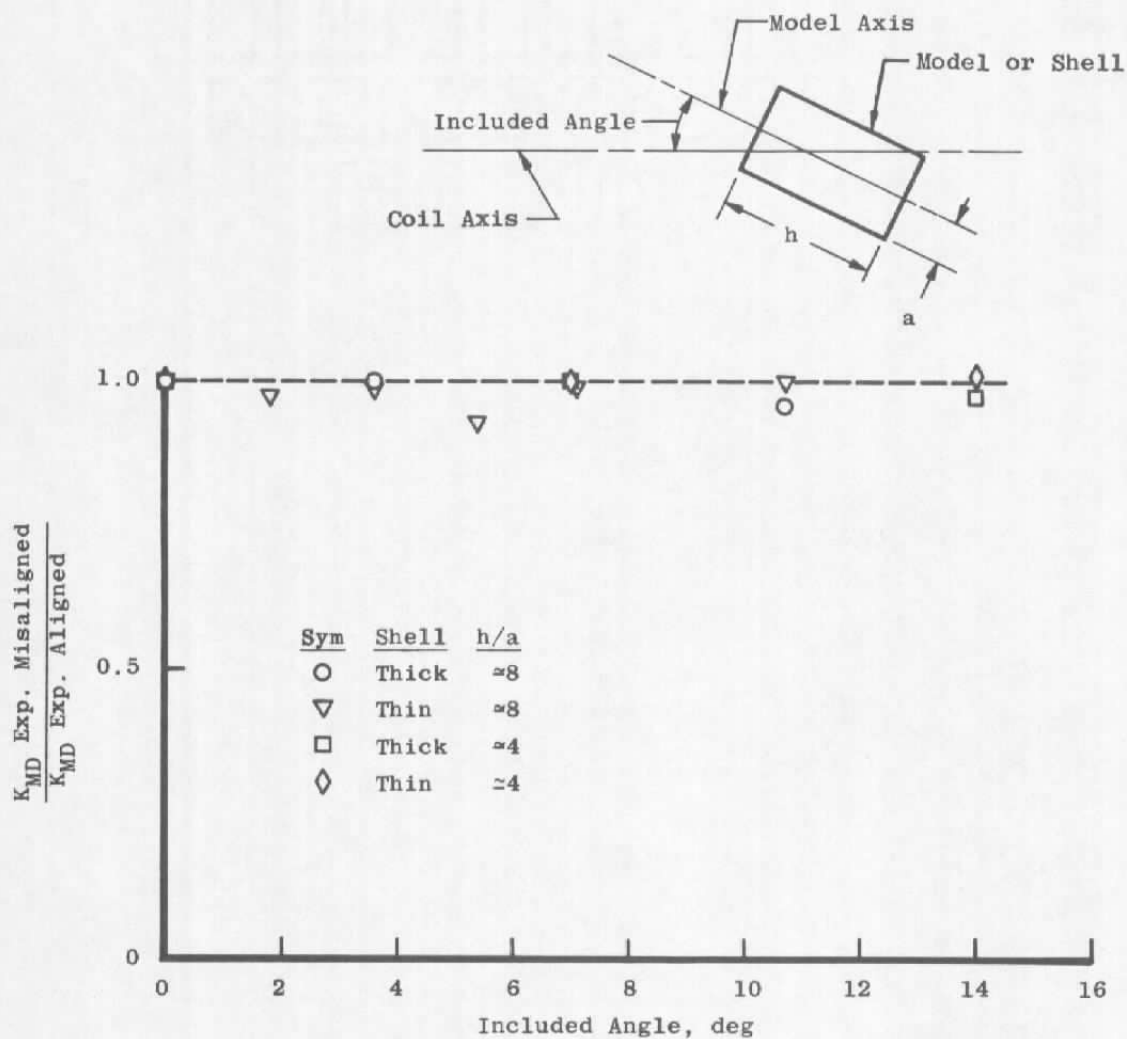
Figure 23. Effect of misalignment on damping coefficient.

APPENDIX A
DERIVATION AND EVALUATION OF SHORT SEGMENT CORRELATION FACTOR

Consider a cylindrical shell of radius (a) and unit length that has been moved from infinity to a distance (r_1) from an infinite line current or an infinite set of transposed line current segments that lie on a z' axis as shown in Figs. A-1a and b. Visualize further that persistent eddy currents were induced in the shell as a result of this action. From Ref. 4, the energy (W') of these eddy currents in terms of their magnetic induction (B') is given by

$$W' = \frac{1}{2\mu_o} \int_\infty (B')^2 \, dv \qquad (A-1)$$

where μ_o is the permeability of free space and v is volume. Next let the cylinder be moved a distance (dr_1) with a corresponding change (dW') in eddy current energy. This change in energy can be equated to mechanical work that was done in the act, i.e.,

$$dW' = F \, dr_1 \qquad (A-2)$$

where F is force per unit length. From this, it is seen that

$$F = dW'/dr_1 \qquad (A-3)$$

or combining with Eq. (A-1) gives

$$F = \frac{1}{2\mu_o} \frac{d}{dr_1} \int_\infty (B')^2 \, dv \qquad (A-4)$$

For near two-dimensional geometry, one can assume that the total field energy is proportional to that within the shell. Therefore by multiplying by an assumed constant of proportionality (K), the integral of Eq. (A-4) need only be over the volume of the cylinder; hence, Eq. (A-4) becomes

$$F = \frac{K}{2\mu_o} \frac{d}{dr_1} \int_{CYL} (B')^2 \, dv \qquad (A-5)$$

If there is to be a perfectly diamagnetic effect (complete shielding inside the shell), then for this space,

$$B' = -B_{INF}$$

or

$$B' = -B_{TRP} \qquad (A-6)$$

where B_{INF} and B_{TRP} are the fields of the parallel line currents or transposed segments as the case may be. Now let a correlation factor $f_{corr}(\Delta, a, r_1)$ be defined such that

$$f_{corr}(\Delta, a, r_1) = F_{TRP}/F_{INF} \qquad (A-7)$$

Combination of Eqs. (A-5), (A-6), and (A-7) then yields

$$\underline{f_{corr}}(\Delta, a, r_1) = \left\{ \frac{d}{dr_1} \int_{CYL} B_{TRP}^2 \, dv \right\} \Bigg/ \left\{ \frac{d}{dr_1} \int_{CYL} B_{INF}^2 \, dv \right\} \qquad (A-8)$$

From Eq. (21) of Ref. 1 and with reference to Fig. (A-1),

$$B_{TRP} = \frac{\mu_0 I}{4\pi r'} \sum_{n=-\infty}^{\infty} (-1)^{n+1} \left\{ \frac{z_1' - n\Delta}{\sqrt{(z_1' - n\Delta)^2 + (r')^2}} - \frac{z_1' - (n-1)\Delta}{\sqrt{[z_1' - (n-1)\Delta]^2 + (r')^2}} \right\} (A-9)$$

where I is the magnitude of current in the line segments, Δ is the segment length, and n represents the nth segment from the point where $z' = 0$. Also from Eq. (22) of Ref. 1,

$$B_{INF} = \frac{\mu_0 I}{2\pi r'} \qquad (A-10)$$

For any given z', it is seen that B_{INF} and B_{TRP} vary only as the magnitude of r' varies so that a geometry suited to the needed integrations is shown in Fig. A-2. To get an average force per unit length in the transposed case, it is necessary to average over one segment length (Δ) at some relatively large z' (see also Fig. 9). Then Eq. (8) for the proposed method of integration becomes

$$f_{corr}(\Delta, a, r_1) = \frac{\left\{ \frac{d}{\Delta dr_1} \int_0^\Delta \int_{r_1-a}^{r_1+a} [B_{TRP}]^2 \, r' \cos^{-1}\left[\frac{(r')^2 + r_1^2 - a^2}{2r'r_1} \right] dr' \, dz' \right\}}{\left\{ \frac{d}{dr_1} \int_{r_1-a}^{r_1+a} [B_{INF}]^2 \, r' \cos^{-1}\left[\frac{r'^2 + r_1^2 - a^2}{2r'r_1} \right] dr' \right\}} \qquad (A-11)$$

The tabulation of a computer program that has been used to solve for $f_{corr}(\Delta, a, r_1)$ is included in Table A-1. The program is truncated at n = 5. A plot of the computed results for a variety of conditions is shown in Fig. A-3 with those for the present experimental situation where $\Delta/a = 4.14$ is shown as the dashed curve. As shown, $f_{corr}(\Delta, a, r_1)$ is quite significant for this value of Δ/a, especially as r_1/a increases. However, for

Δ/a values on the order of sixty, as would be the case in an actual range guidance system, $f_{corr}(\Delta, a, r_1)$ approaches unity for expected values of r_1/a. Hence, in most actual range applications, the idealized theory of Ref. 1 should be adequate without $f_{corr}(\Delta, a, r_1)$ being needed.
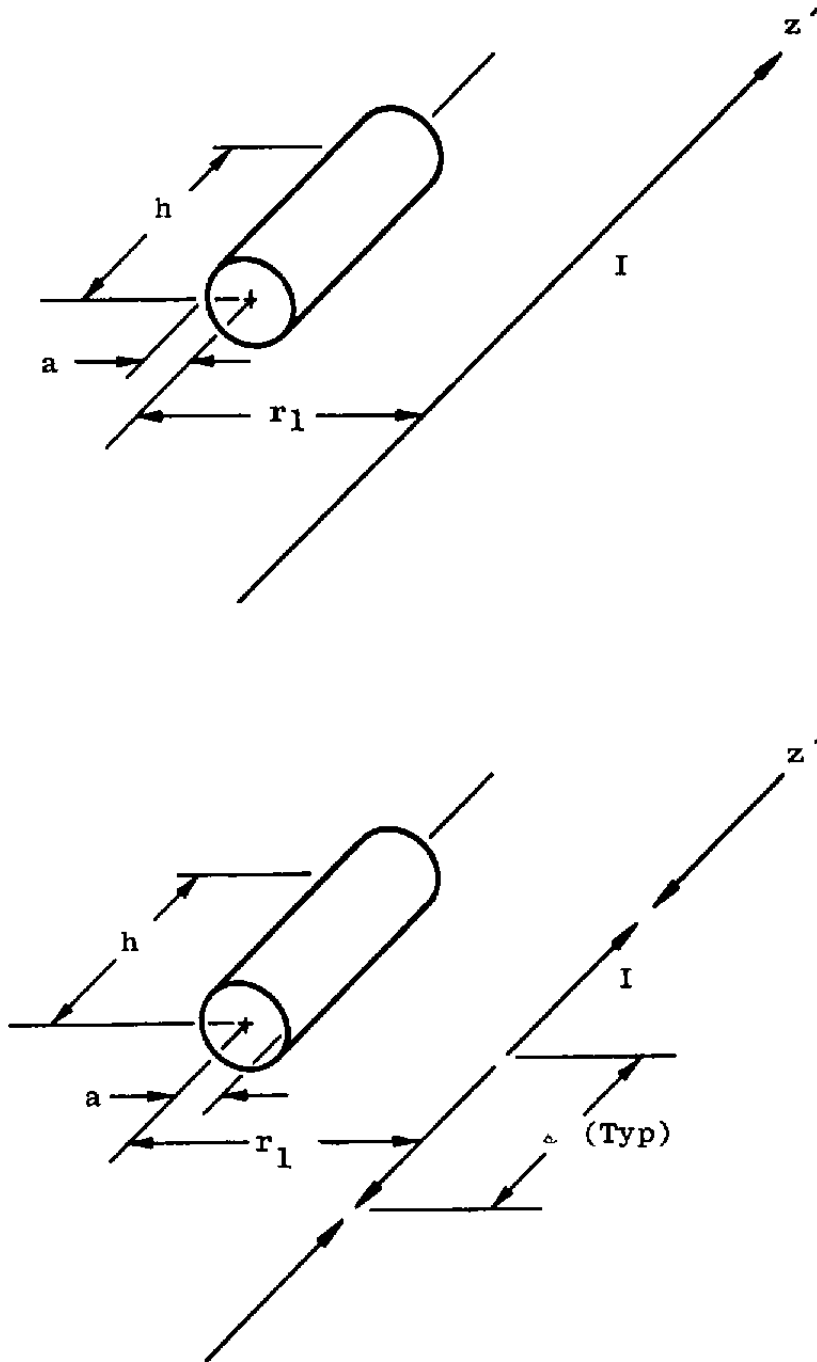
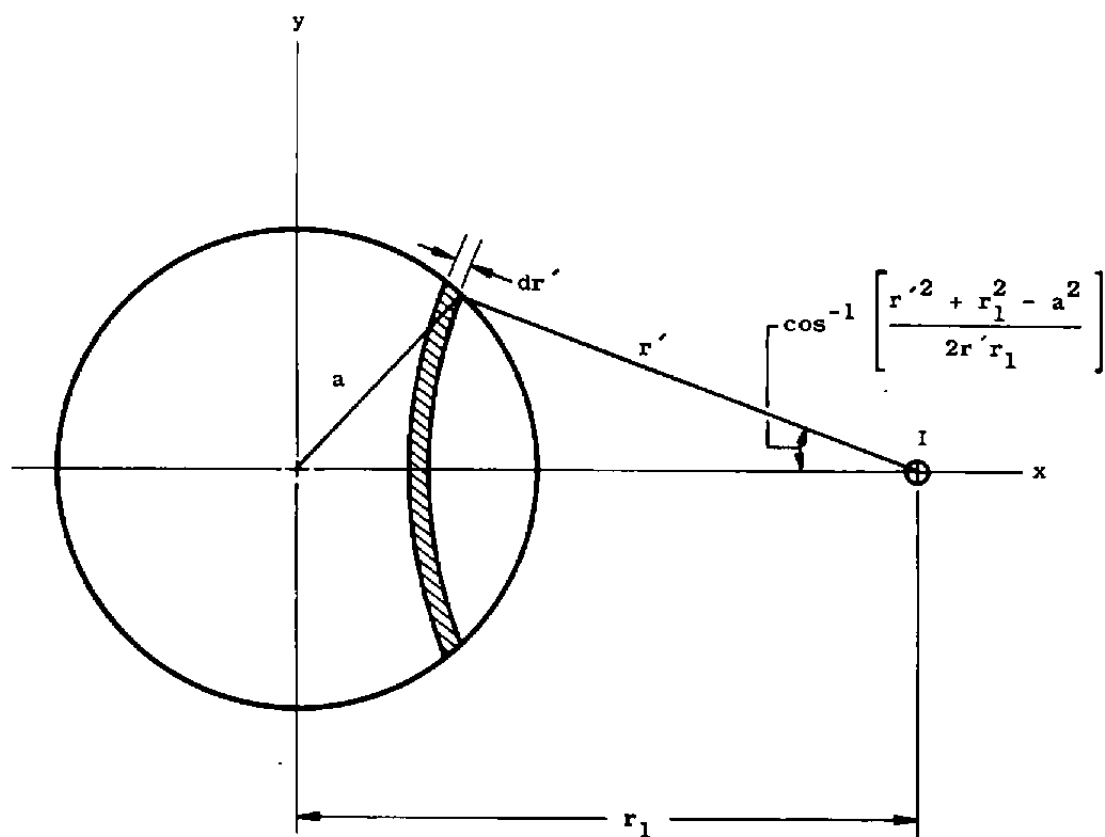Figure A-1. Nomenclature for cylindrical shell and currents.

Figure A-2. Geometry for integration.
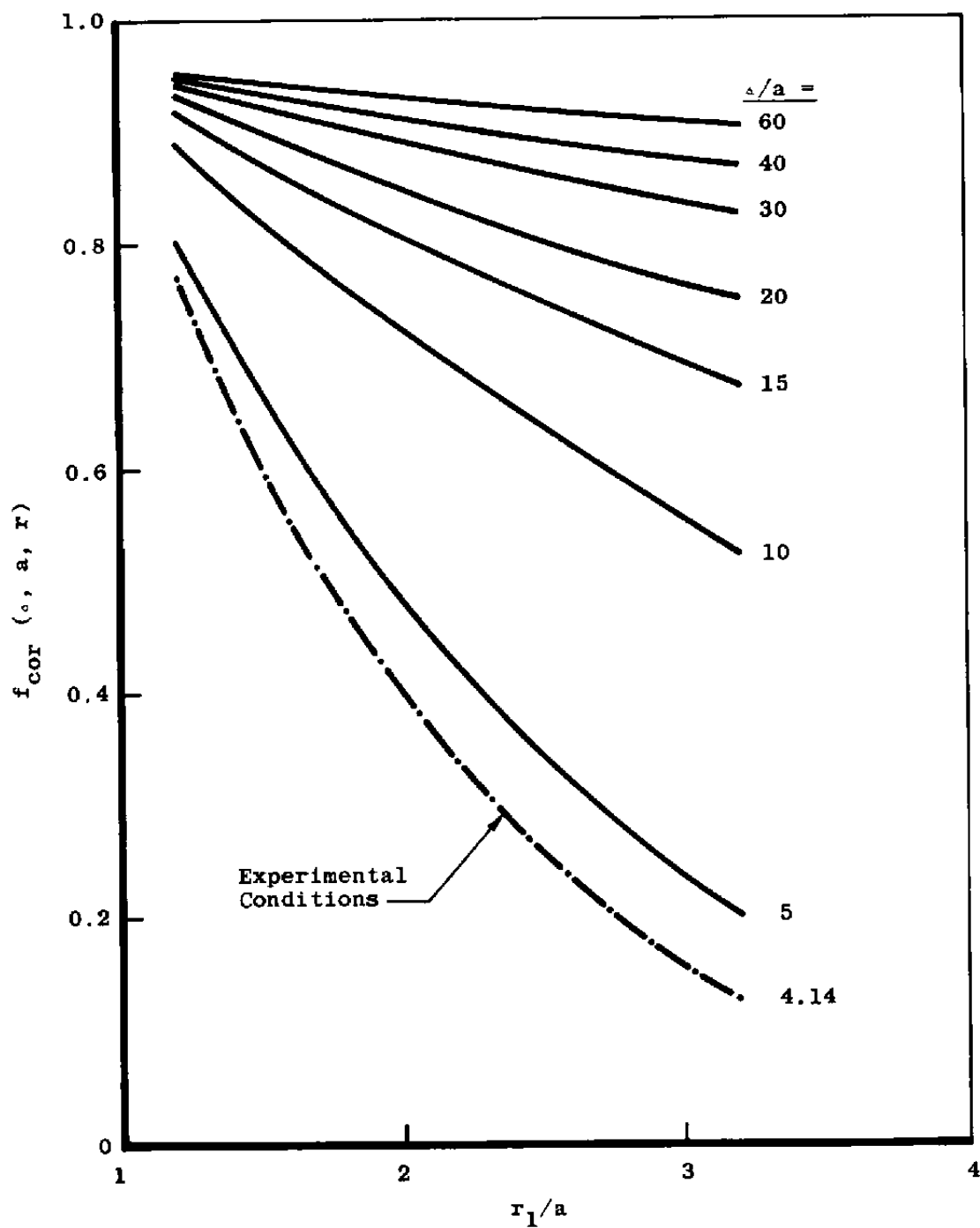
Figure A-3. Correlative factor versus r_1/a.

Table A-1.

```
C     **************************************************************
C     **                                                          **
C     **                 FORTRAN PROGRAM                          **
C     **                                                          **
C     **                    FOR                                   **
C     **                                                          **
C     **          SHORT SEGMENT CORRELATION FACTOR               **
C     **                                                          **
C     **************************************************************
C
C     THIS PROGRAM FINDS THE RATIO OF THE DERIVATIVES OF TWO INTEGRALS
C     DO LOOP 1 EVALUATES A SUMMATION FOUND IN THE INTERGRAL IN THE NUMERATOR
C     DO LOOP 2 STEPS IN THE Z DIRECTION
C     DO LOOP 3 STEPS IN THE R' DIRECTION
C     DO LOOP 4 STEPS R1 A SMALL AMOUNT FOR CALCULATION OF DERIVATIVE
C     DO LOOP 5 STEPS IN THE R1 DIRECTION
C     DO LOOP 100 STEPS THE PROGRAM THROUGH DIFFERENT S TO A RATIUS
C
C
        DIMENSION    ANUM(2),ADEN(2)
C A IS THE EFFECTIVE RADIUS OF MODEL
        A =.02413
        DO 100 K=20,60,10
        AAA=K
C  S IS THE LENGTH OF A TRANSPOSED SEGMENT
        S=AAA*A
        DR1=.1*A
        DO 5 I= 1,21
        A5=I-1
        R1=1.2*A+A5*DR1
        ROA=R1/A
        DR11=.01*A
        DO 4 J=1,2
        A4= J-1
        R1=R1+A4*DR11
        V1=.0
        V2=.0
        DRPR=.025*A
        RPR=R1-A-DRPR
        DO 3 M=1,81
        RPR=RPR+    DRPR
        DZ=.025*S
        ZPR=4.0*S-DZ
        DO 2 L=1,21
        ZPR=ZPR+DZ
        FN2=.0
        DO 1 N=1,9
        A1=N
        FN1=((-1.)**(N+1))*((ZPR-A1*S)/SQRT((ZPR-A1*S)**2+RPR
       1**2)-(ZPR-(A1-1.)*S)/SQRT((ZPR-(A1-1.)*S)**2+RPR**2))
    1   FN2= FN2+FN1

        BNTRP=FN2/(2.*RPR)
        BNINF=1./RPR
        COMON=RPR*ARCOS(((RPR**2)+(R1**2)-(A**2))/(2.*RPR*R1))
        V=(BNTRP**2)*COMON*DZ*DRPR
        V1=V+V1
        B=(BNINF**2)*COMON*DZ*DRPR
    2   V2=B+V2
    3   CONTINUE
        ANUM(J)=V1
    4   ADEN(J)=V2
        CF= (ANUM(2)-ANUM(1))        /  (ADEN(2)-ADEN(1))
        RES=S/A
    5   PRINT 20,RES,ROA,CF
   20   FORMAT('0 S/A  ',E12.4,'0  R/A  ',E20.12,'  CORRELATION PARAMETER
       1      ',E20.12)
  100   CONTINUE
        STOP
        END
/*
```

APPENDIX B
METHODOLOGY FOR EXTRACTION OF EXPERIMENTAL DAMPING COEFFICIENTS

In the case of a pendulum such as the one shown in Fig. B-1, its motion is the result of two types of forces. One is positional in nature and is the resultant of the gravitational force acting on the pendulum (at its center of gravity, c_g) and the tension in its support rod (or pendulum arm). As shown in the figures, this force has a magnitude of Mg sin θ where M is the mass of the pendulum, g is the acceleration due to gravity, and θ is the angular position of the pendulum with respect to the Earth's vertical. In the case where θ is small, sin $\theta \simeq \theta$, and the restoring force is seen to have a magnitude of Mgx/ℓ where ℓ and x are apparent in Fig. B-1.

The other forces acting on the pendulum are frictional in nature and vary with the pendulum's angular velocity ($d\theta/dt$) where t is time. These forces arise from numerous sources. The dominant ones in the present case arise from air resistance and magnetic forces acting at the center of magnetic pressure. Since these magnetic forces act on that portion of the body which is displaced by an amount (x'), rather than x, the velocity (dx'/dt) determines the magnetic damping. As shown in Fig. B-1, dx'/dt is equal to (ℓ_M/ℓ)dx/dt, where ℓ_M is apparent from the figure, so that the frictional forces must have a magnitude of $[(\ell_M/\ell) K_{MD} + C_D](dx/dt)$ where K_{MD} is the magnetic damping coefficient and C_D is predominantly the aerodynamic drag coefficient but includes all other effects with the exception of magnetic ones.

The equation of motion of the pendulum is given by Newton's second law so that

$$M \frac{d^2x}{dt^2} = - \frac{Mgx}{\ell} - \left(\frac{K_{MD} \ell_M}{\ell} + C_D \right) \frac{dx}{dt} \tag{B-1}$$

Since the pendulum displays damped harmonic motion, the solution of interest is

$$X = A \left\{ \exp\left[-(K_{MD} \ell_M/\ell + C_D)(t/2M) \right] \right\} \cos(\omega t - \delta) \tag{B-2}$$

where A is an arbitrary constant, ω is equal to

$$\sqrt{g/\ell - \left[(K_{MD} \ell_M/\ell + C_D)/2M \right]^2}$$

and δ is a possible angular displacement.

It is, therefore, possible to find the value of $K_{MD} \ell_M/\ell + C_D$ by observing the motion of the pendulum. The damped motion is typified by that suggested in Fig. B-2

so that it is possible to eliminate concern over the cosine term by measuring the displacement (x) at times when $\cos(\omega t - \delta)$ has the value of unity; i.e., at the extremes of the oscillatory motion. Then, it is simply a matter of measuring the magnitude of x at two such occasions and recording the time interval between them to have all information needed to calculate $K_{MD}\ell_M/\ell + C_D$.

By arbitrarily assigning the zero value to the time of the initial measurement,

$$X_1 = A \exp\left[-(K_{MD}\ell_M/\ell + C_D)t_1/2M\right]\Bigg|_{t_1=0} = A \qquad (B\text{-}3)$$

the weighing factor (A) can be determined. Then,

$$X_2 = X_1 \exp\left[-(K_{MD}\ell_M/\ell + C_D)\Delta t/2M\right] \qquad (B\text{-}4)$$

and since $(K_{MD}\ell_M/\ell + C_D)$ remains the only unknown, algebraic manipulation yields

$$\frac{K_{MD}\ell_M}{\ell} + C_D = \frac{2M}{\Delta t} \ln \frac{X_2}{X_1} \qquad (B\text{-}5)$$

The coefficient C_D can be determined at a time when K_{MD} is zero from the expression

$$C_D = \frac{2M}{\Delta t} \ln \frac{X_2}{X_1} \qquad (B\text{-}6)$$
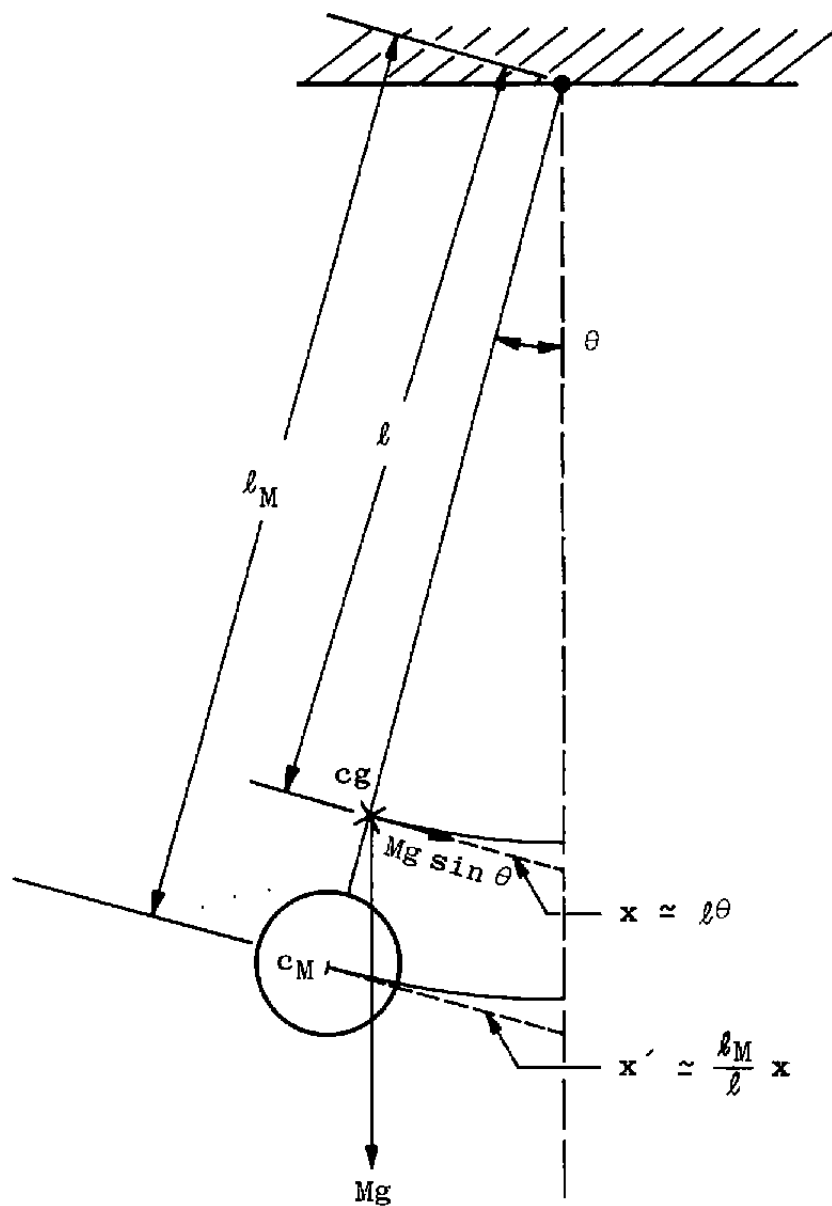
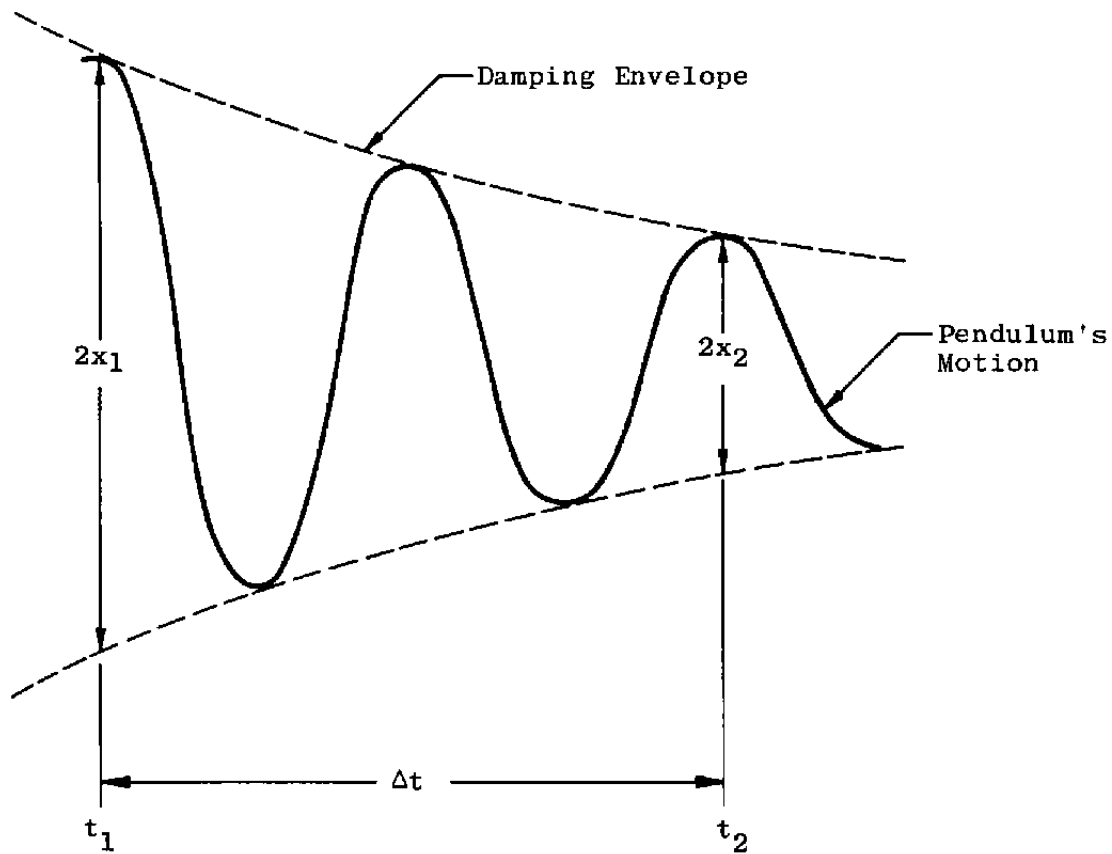Figure B-1. Pendulum nomenclature.

Figure B-2. Damped motion of pendulum.

NOMENCLATURE

a   Radius of conductive shell or projectile forebody, m

B   Magnetic induction, Wb/m^2

b   Distance from z-axis to guideway line currents, m

c_M Effective center of magnetic forces

c_g Center of mass

c_p Center of aerodynamic pressure

F   Force per unit length, N/m

f_{corr} Correlation parameter

g   Acceleration of gravity, m/sec^2

h   Length of conductive shell, m

I   Electric current, amp

K_M Magnetic positional force constant, N/m

K_{MD} Magnetic damping force constant, N-sec/m

ℓ Moment arm for aerodynamic forces, m

ℓ_M Moment arm for magnetic forces, m

M   Pendulum's mass, kg

n   nth current segment

$\mathcal{R}$ Radial position of projectile's axis with respect to guideway axis, m

r   Radial distance from axis of projectile or other reference to item or point of interest, m

69

δ	Shielding ratio (see Eqs. (1) and (2))
α	Guideway current segment length (see Fig. 1), m
t	Time, sec
$\overline{V}$	Velocity of projectile's c_g, m/sec
W	Energy of eddy currents induced in shell, J
x	Cartesian coordinate, m
y	Cartesian coordinate, m
ψ	Dispersion of projectile's c_g from z-axis, m
z	Cartesian and/or polar coordinate (coincident with the range and guideway axis), m
z'	Offset z-axis, m
a	Angle of attack, rad
β	Angular position of shell referenced to x-axis, rad
γ	Angle between V and Z-axis, rad
δ	Phase angle, rad
ϵ	Phase lag between inducing field and field of eddy currents, rad
μ	Permeability, h/m
ρ	Volume resistivity, ohm-m
ς	Area resistivity, ohm
Ω	Ohm
ω	Angular frequency, rad/sec

Subscripts

D	Damping field, currents, forces, etc.
DRG	Drag
g	Gravity
INF	Infinite
M	Magnetic (positional)
MD	Magnetic damping
M$\mathcal{R}$	Radial M
Mβ	Angular M
MD$\cdot\mathcal{R}$	Radial MD
MDβ	Angular MD
n	nth segment
o	Refers to conditions of free space
P	Positional field, currents, forces, etc.
p	Pressure
$\mathcal{R}$	Radial component
r	Radial direction with respect to currents
s	Source
TRP	Transposed
β	Angular component

Superscripts

'   Implies an offset system of polar coordinates